Myosin-X-dependent assembly of the extracellular matrix limits breast cancer invasion.

Emilia Peuhu[1,2,*], Guillaume Jacquemet[2-4,*], Colinda LGJ Scheele[5,6], Ilkka Paatero[2], Kerstin Thol[2], Aleksi Isomursu[2], Maria Georgiadou[2], Camilo Guzmán[2], Satu Koskinen[2], Asta Laiho[2], Laura L Elo[1,2,7], Pia Boström[8,9], Pauliina Hartiala[9,10], Jacco van Rheenen[5], and Johanna Ivaska[2,7,11, ✉]

[1]Institute of Biomedicine, FICAN West Cancer Laboratory, University of Turku, FI- 20520 Turku, Finland.
[2]Turku Bioscience Centre, University of Turku and Åbo Akademi University, FI- 20520 Turku, Finland.
[3]Åbo Akademi University, Faculty of Science and Engineering, Biosciences, FI- 20520 Turku, Finland.
[4]Turku Bioimaging, University of Turku and Åbo Akademi University, FI- 20520 Turku, Finland.
[5]Division of Molecular Pathology, Oncode Institute-Netherlands Cancer Institute, 1066CX Amsterdam, Netherlands.
[6]VIB-KU Leuven Center for Cancer Biology, Department of Oncology, Leuven, Belgium.
[7]InFLAMES Research Flagship Center, University of Turku, FI- 20520 Turku, Finland.
[8]Department of Pathology, Turku University Hospital, FI- 20520 Turku, Finland.
[9]University of Turku, FI- 20520 Turku, Finland.
[10]Department of Plastic and General Surgery, Turku University Hospital, FI- 20520 Turku, Finland.
[11]Department of Life Technologies, University of Turku, FI- 20520 Turku, Finland.
[*]equal contribution

The mechanisms triggering the transition from in situ tumors to invasive carcinomas are poorly understood. The process involves breaching tumor-containing basement membranes (BM) and cancer cell invasion into the tumor stroma. Myosin-X (MYO10) is a filopodia-inducing protein frequently overexpressed in metastatic breast cancer. Here, we investigated the contribution of MYO10 to invasive breast tumor progression. We found that downregulation of MYO10 expression reduces breast cancer cell protrusions and migration *in vitro*. In addition, it attenuates protrusive activity and cell motility in early-stage breast cancer xenografts, which is in line with MYO10's established pro-invasive function. However, MYO10 depletion also promoted the local dispersal of increasingly basal-like tumor cells into the tumor stroma *in vivo*, resembling the transition from in situ to invasive tumors. MYO10-depleted tumors exhibited compromised BM structures, which correlated with increased mRNA expression but the reduced assembly of BM proteins surrounding the xenograft. Furthermore, MYO10-depleted 3D spheroids were defective in extracellular matrix (ECM) assembly around the spheroids, indicating a functional role for MYO10 in ECM deposition. Altogether, our data support a model where tumor cell protrusive activity, induced by MYO10, contributes to anti-invasive ECM organization at the in situ stages of breast cancer but promotes cell motility in advanced invasive breast cancer.

DCIS, breast cancer, filopodia, MYO10, basement membrane
Correspondence: *johanna.ivaska@utu.fi*

Introduction

Despite recent therapeutic advances, breast cancer remains a significant cause of death among women (Ferlay et al., 2018). Breast cancer is particularly impervious to established therapies at later stages of the disease when tumors have become invasive and metastatic. A critical step promoting the transition from a non-invasive to an invasive tumor involves cancer cells breaching their basement membrane (BM) barrier and invading into the surrounding stroma, either as single cells or as a stream (Clark and Vignjevic, 2015). Therefore, understanding how cancer cells interact with and breach the BM is of high clinical and therapeutic interest.

BMs are thin, dense sheets of specialized extracellular matrix (ECM) molecules surrounding epithelial tissues (Yurchenco and Patton, 2009). They are composed of a three-layer ECM network, the inner layer mainly containing laminins and the outer layer formed of type IV collagen. These two layers are interlinked by several additional ECM molecules, including nidogen, lumican, and perlecan. BMs are effective biological barriers maintained by constant turnover and remodeling of ECM components (Matsubayashi et al., 2020; Keeley et al., 2020). In addition, BMs regulate epithelial architecture by establishing polarity and by providing survival cues and mechanical support.

Cancer cells can utilize specialized protrusions, such as invadopodia, to traverse BMs (Eddy et al., 2017). Invadopodia contain proteases that can degrade ECM molecules, releasing pro-invasive soluble cues and promoting the transition from in situ to invasive breast carcinoma (Lodillinsky et al., 2016; Ferrari et al., 2019; Monteiro et al., 2013). In addition, stromal cells may facilitate cancer cell invasion by physically remodeling BMs (Glentis et al., 2017). To date, most of the research has focused on elucidating the mechanisms by which cancer cells breach established BMs. In contrast, very little is known about how cancer progression is coupled to general BM alterations and whether cancer cells themselves could contribute to BM assembly and maintenance.

Filopodia are small and dynamic finger-like actin-rich protrusions that are often the first point of contact between a cell and its immediate surroundings. Filopodia contain cell-surface receptors, such as integrins, cadherins, and growth factor receptors that can interact with and interpret a wide variety of cues (Jacquemet et al., 2019; Fierro-González et al., 2013; Valenzuela and Perez, 2020). Accordingly, filopodia-like protrusions are widely used by cells *in vivo* during nor-

mal processes, such as development, angiogenesis, immune surveillance, and wound healing (Jacquemet et al., 2015). Filopodia-like protrusions are also associated with increased invasion and metastasis in several cancer types and have been implicated in supporting cancer cell survival at metastatic sites (Shibue et al., 2012, 2013; Jacquemet et al., 2017).

Several filopodia-inducing proteins, such as the molecular motor myosin-X (MYO10) or the actin-bundling protein fascin, promote cancer cell invasion *in vitro* and *in vivo* and are associated with poor patient prognosis in multiple carcinomas (Arjonen et al., 2014; Cao et al., 2014; Li et al., 2014; Tokuo et al., 2018). For example, upregulation of MYO10 in metastatic, p53 mutant breast cancer was reported to increase filopodia formation, invasion, and metastasis and to correlate with poor patient outcomes in a large cohort of breast cancer patients (Arjonen et al., 2014). As another example, Fascin is highly expressed at the invasive front of several epithelial carcinomas and has been implicated in promoting pancreatic cancer metastasis (Li et al., 2014; Vignjevic et al., 2007; Huang et al., 2015).

Filopodia are relatively well-defined structures in cells on 2D substrates (Jacquemet et al., 2019). Similarly, in 3D substrates and *in vivo*, cells can form filopodia-like protrusions (for instance, (Jacquemet et al., 2013; Millard and Martin, 2008; Liu et al., 2018). However, it is often unclear how these structures compare to the filopodia described in 2D and how they contribute to cancer cell invasion. Furthermore, much of the research on cell protrusions in cancer has focused on cancer cell-intrinsic properties facilitating migration, invasion, and navigation through the complex 3D stroma. The possibility of cell protrusions regulating different aspects of the tumor microenvironment during cancer progression, on the other hand, is not well understood.

Here we report that MYO10 has an unexpected tumor-limiting function at an early, non-invasive stage of breast cancer xenografts. We find that MYO10 is expressed in human ductal carcinoma in situ (DCIS) and that MYO10 depletion in a xenograft model of breast cancer progression compromises BM formation around the tumor acini resulting in the dispersal of increasingly basal-like carcinoma cells into the surrounding stroma. Furthermore, *in vitro* and ex-vivo imaging experiments demonstrate that MYO10-regulated protrusions contribute mechanically to ECM assembly. Our data support a model where MYO10-dependent tumor cell protrusions modulate ECM assembly at the tumor-stroma interface in early-stage breast cancer to limit cancer progression.

Results

MYO10 contributes to filopodia formation and collective cell migration *in vitro*. MYO10 is highly expressed in a subset of breast carcinomas with a poor prognosis (Arjonen et al., 2014). However, MYO10 expression at the early, non-invasive-stage of breast cancer has not been investigated. We detected MYO10 mRNA expression in situ in patients diagnosed with pre-invasive DCIS with an intact BM (Fig. 1A and Fig. S1), indicating that MYO10 may also play a role in the early stages of tumor progression. To investigate this

possibility, we turned to a cellular model (MCF10DCIS.com cells) that recapitulates the different stages of tumor progression when grafted in mice and mimics the progression of the human disease with a predictable timeline (Frittoli et al., 2014; Miller et al., 2000). In line with previous reports, ten days post-injection MCF10DCIS.com cells formed acini surrounded by a BM with no visible incursion into the surrounding stroma. By day 25, some acini had visibly started to invade (Fig. S2A).

Previously we have shown that MCF10DCIS.com cells produce high numbers of filopodia as they invade collectively *in vitro* (Jacquemet et al., 2017). To investigate any MYO10 dependency in generating these filopodia, we silenced MYO10 expression using short hairpin RNA (shRNA). Subsequently, we pooled four MYO10-depleted single-cell clones to create the shMYO10 DCIS.com cell line used in this study (Fig. 1B and Fig. S2B-F). Silencing of MYO10 led to a marked reduction in filopodia density and length in migrating cells (Fig. 1C) and decreased cell invasion speed through collagen in a 2D overlay assay (Fig. 1D and Video 1). Furthermore, high-resolution live-cell imaging revealed that, in the absence of filopodia, shMYO10 cells switch to a lamellipodia-driven mode of collective cell migration (Fig. 1E and Video 2). To investigate this further, we mixed shCTRL, and shMYO10 cell lines (alternating GFP labeling of the cell lines) (Fig. S3A) and recorded cell migration live. shMYO10 cells consistently lagged behind the shCTRL cells, which preferentially localized to the front of the collectively migrating cell layer (Fig. S3B-C and Video 3). These data indicate that MYO10 contributes to filopodia formation and efficient cell motility in MCF10DCIS.com cells *in vitro*.

MYO10 depletion accelerates the loss of non-invasive xenograft morphology in vivo. Since MYO10 has been previously implicated in supporting cell division (Sandquist et al., 2018), we assessed the contribution of MYO10 to MCF10DCIS.com cell proliferation *in vitro* and *in vivo*. MYO10 silencing did not affect MCF10DCIS.com growth in 2D culture (Fig. S4A), and the size and weight of shCTRL or shMYO10 xenograft tumors were comparable (Fig. S4B-C). However, MYO10-silenced cells formed larger organoids when grown in 3D (Fig. S4D-E), and BrdU labeling indicated increased rather than decreased cell proliferation in shMYO10 tumors 25 days post-injection in mice (Fig. S4F-G). Thus, MYO10 is not required for DCIS.com cell proliferation, and the silencing of MYO10 may even modestly accelerate DCIS.com cell proliferation in 3D environments.

Next, we compared the onset of invasion in shCTRL and shMYO10 xenografts by blind scoring of the tumor histology. As expected, at 25 days post-inoculation (Fig. S2A), shCTRL tumors were composed of DCIS-like acini or acini exhibiting partial invasion (Fig. 2A-B). In contrast, most shMYO10 tumors displayed partial or complete invasion leading to loss of the in situ tumor organization (Fig. 2A-B). Interestingly, tumors formed by mixing shCTRL and shMYO10 cells in equal proportions displayed an intermediate phenotype, suggesting a dose-dependent effect
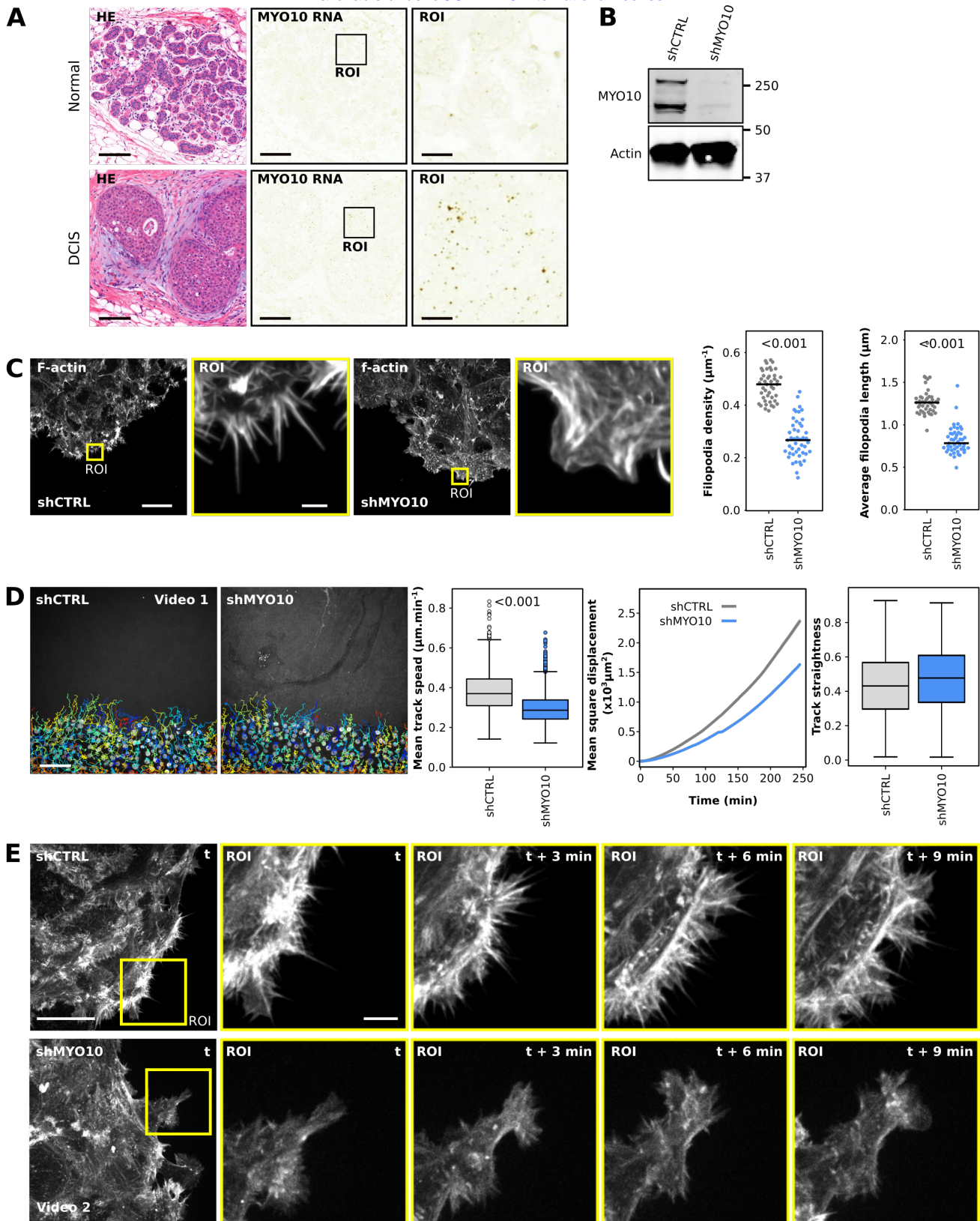
Fig. 1. MYO10 modulates filopodia formation and collective cell migration in DCIS.com cells. (**A**): In situ labeling of MYO10 mRNA in normal and DCIS regions of a human breast sample (images representative of 4 patient samples per condition). MYO10 mRNA can be visualized by the dots visible in the magnified ROI. Scale bars: (main) 100 μm; (inset) 20 μm. (**B**): shCTRL and shMYO10 DCIS.COM cells were lysed, and MYO10 protein levels were analyzed by western blot. (**C**): shCTRL and shMYO10 DCIS.COM cells were left to migrate underneath a collagen gel for two days (d), fixed, stained, and imaged using a spinning-disk confocal microscope. A representative field of view is displayed. Yellow squares highlight regions of interest (ROIs) that are magnified. Scale bars: (main) 25 μm; (inset) 2 μm. Filopodia density and the average filopodia length were analyzed using FiloQuant. Results are displayed as dot plots (n > 45 fields of view analyzed per condition; three independent experiments; randomization test). (**D**): shCTRL and shMYO10 DCIS.COM cells were left to migrate underneath a collagen gel for 1 d, incubated with SiR-DNA (to visualize nuclei), and imaged live using a spinning-disk confocal microscope (20x air objective). Cells were then automatically tracked using StarDist and TrackMate. A representative field of view with cell tracks is displayed (See also Video 1). Mean track speed, mean square displacement, and track straightness were calculated using the motility lab website (three independent experiments, 30 fields of view per condition, and n > 2300 cell tracks; randomization test). Scale bar: 100 μm. (**E**): shCTRL and shMYO10 DCIS.COM cells were left to migrate into a collagen gel for 1 d and imaged live using a spinning-disk confocal microscope (100x objective). A representative field of view with selected time points is displayed (See also Video 2). Scale bars: (main) 25 μm; (inset) 5 μm.

(Fig. S4H).

Breast cancer is a heterogeneous disease with different subtypes that exhibit features of the luminal and basal cell types that form the mammary gland and a varying degree of epithelial to mesenchymal transition that has been associated with increased tumor invasion. Immunostaining of the DCIS.com breast cancer xenografts with markers for luminal-like (keratin 8; KRT8) and mesenchymal/basal-like breast cancer cells (vimentin; VIM and the transcription factor Slug; SNAI2) revealed a notable presence of cells with mesenchymal traits particularly at the perimeter of MYO10-depleted xenografts (Fig. 2C-F). Inclusion of additional basal markers, α6 integrin and α smooth muscle actin (αSMA/ACTA2) that were clearly expressed at the edges of shCTRL and shMYO10 tumors, further validated the observation that basal-like cells were distributed over a broader margin at the edges of shMYO10 tumor acini (Fig. 2G-H). Thus, MYO10 depletion leads to an increased presence of tumor cells with mesenchymal/basal-like features that may be the cause or the consequence of the faster onset of tumor invasion in MYO10-depleted tumors.

Next, we investigated where MYO10-depleted cells localize with respect to shCTRL cells in the xenografts in mice grafted with a 50:50 mixture of shCTRL and shMYO10 cells (GFP expressed in either shCTRL or shMYO10 cells). We used two-photon intravital microscopy (Fig. 2I) and tumor histology (Fig. 2J) to investigate the differential behavior between shCTRL and shMYO10 cells within the same tumor. Importantly, in the mixed scenario, tumor growth and invasion was comparable in all tumors and invasion was enhanced compared to shCTRL tumors (Fig. S4H-I). In line with the more dispersed and basal-like phenotype of tumors composed of shMYO10 cells alone (Fig. 2C-H), we observed preferential segregation of shMYO10 cells to the basal position, i.e., the edges of the tumor acini when they were mixed with shCTRL cells (Fig. 2I-K and Videos 4-5). Altogether, these data demonstrate that MYO10-depletion promotes basal cell features and basal localization of tumor cells *in vivo* and indicates a role for MYO10 in supporting the retention of in situ tumor organization in early-stage breast cancer xenografts.

MYO10 promotes basement membrane assembly in vivo. As breaking through the BM membrane is a critical step in tumor progression, we next examined the BM of tumor xenografts at day 25 in more detail (Fig. 3A-D). Tumors formed by shCTRL cells were surrounded by a collagen IV-positive BM. In contrast, the BM around shMYO10 tumors was harder to detect and exhibited decreased collagen IV staining (Fig. 3A-C). BMs contribute to the assembly of other ECM scaffolds, including the proper assembly of fibronectin fibrils (Lu et al., 2020). In line with this notion, we observed that the fibronectin matrix in shMYO10 tumors were less developed, and the ECM surrounding the tumors contained less fibronectin than the shCTRL tumors (Fig. 3B-C).

A similar defect in collagen IV deposition around shMYO10 acini was apparent at an earlier stage of tumor development when the acini form (10 days post-inoculation)

(Fig. 3C). While fibronectin staining appeared equal in shCTRL and shMYO10 tumors, visible fibronectin fibrils were mostly absent in shMYO10 acini (Fig. S5). Instead, bright fibronectin puncta, which are reminiscent of folded fibronectin not yet assembled into filaments, could be observed at the edges of shMYO10 acini.

The apparent lack of BM assembly in the MYO10-depleted tumors was further investigated with electron microscopy (EM). In negatively-stained EM, BMs were visible (as dark fibers) at the edges of shCTRL acini but could not be easily observed in shMYO10 tumors (Fig. 3E). Moreover, occasional filopodia-like protrusions were observed at the edge of the shCTRL, but not in shMYO10 DCIS-like xenografts, *in vivo* using EM (Fig. 3F). Taken together, these data indicate that the BM of shMYO10 acini is already defective while the tumors are forming and point to inadequate BM production or assembly rather than degradation, which typically occurs at a much later stage in tumor progression (Lodillinsky et al., 2016).

ECM production is up-regulated in shMYO10 tumors. To investigate the expression of BM components, we performed bulk mRNA sequencing of shCTRL and shMYO10 tumors (at 25 days post-inoculation), taking care to distinguish gene expression changes in the tumor (human genes) and the stroma (mouse genes) (see methods for details). MYO10 expression was decreased in shMYO10 tumors, validating our approach (Fig. S6A). Overall, stromal gene expression profiles were nearly identical in shCTRL and shMYO10 tumors (Fig. 4A). In contrast, gene expression profiles of shCTRL and shMYO10 tumors were distinct, with many differentially expressed genes detected between the tumors (Fig. 4B and table S1). Interestingly, expression of the filopodia-inducing proteins FMNL3 and neurofascin were increased in shMYO10 tumors, indicating a possible compensatory mechanism to promote filopodia formation when MYO10 is down-regulated (Fig. S6B and Fig. S6C).

Expression of several ECM molecules, including collagen IV (COL4A1, COL4A2, COL4A5, and COL4A6), collagen VI (COL6A1), laminin (LAMA1), and fibronectin (FN1), were increased in shMYO10 tumors (Fig. 4C and Fig. S6C), which was unexpected considering the inadequate BM generation of these tumors (Fig. 3). Furthermore, gene ontology analyses and annotation of our dataset using the Matrisome database (Naba et al., 2012, 2016, 2017) confirmed that MYO10-depleted xenografts produce more ECM proteins overall (Fig. 4D and 4E). Thus, MYO10 depletion does not reduce BM component production but instead leads to an overall increase in ECM production *in vivo*.

MYO10 filopodia promote ECM assembly in 3D. Next, we assessed whether MYO10 contributes to ECM assembly by imaging spheroids grown in Matrigel and incubated with fluorescently labeled ECM molecules (Fig. S7A). We observed a fine layer of ECM surrounding the spheroids, immediately adjacent to the outermost cells with filopodia protruding through it (Fig. 5A-B and S7B). This ECM layer did not appear to be continuous but instead to form plaques that
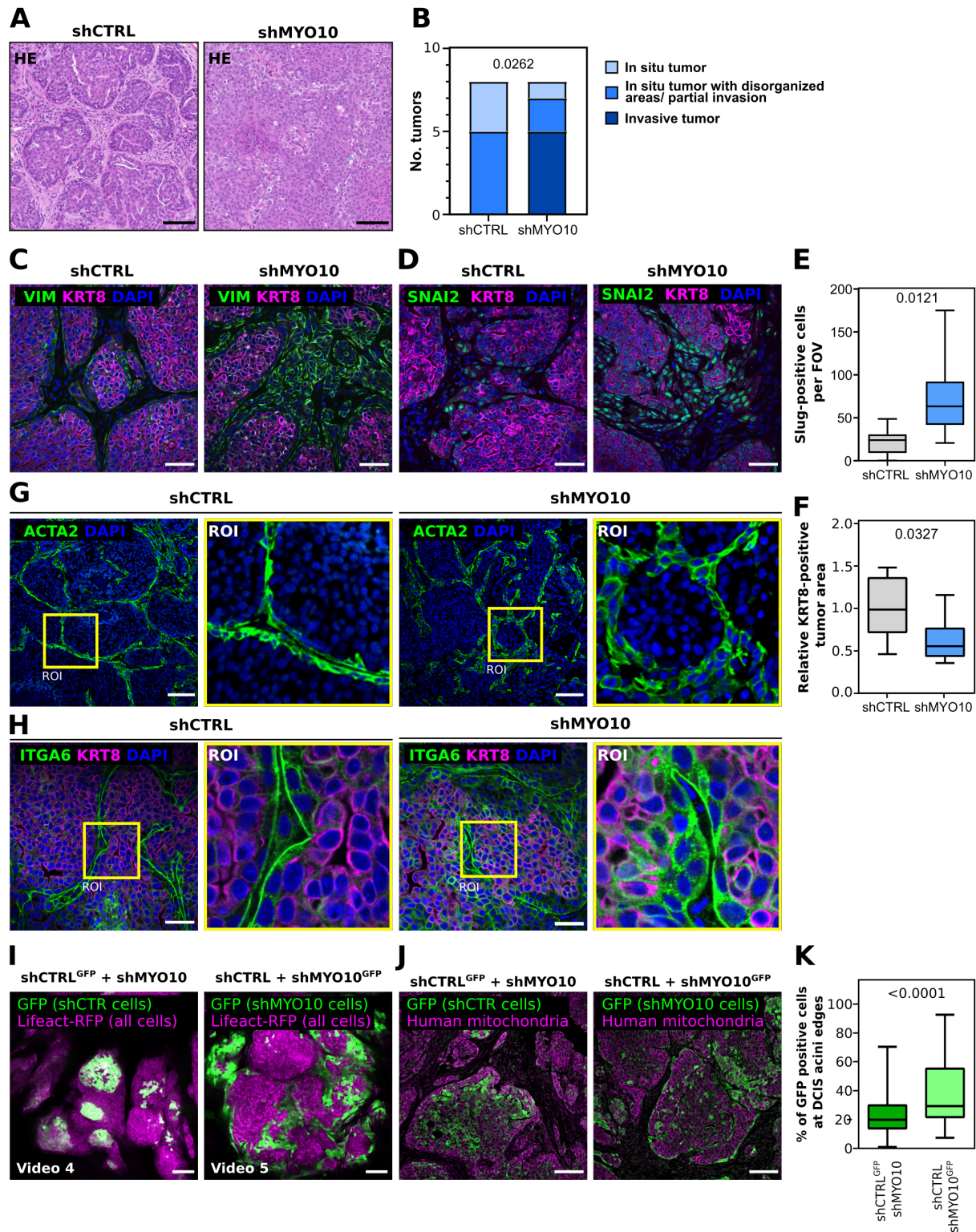
Fig. 2. MYO10 depletion induces the dispersal of increasingly basal-like tumor cells into the tumor stroma *in vivo*. (**A-H**): shCTRL and shMYO10 cells were injected subcutaneously in NOD.scid mice. At 25 days post-injections, tumors were dissected, and tissue sections were stained as indicated and imaged. (**A**) Representative images of tumor histology and (**B**) quantification of DCIS invasion are shown (n = 8 tumors, Chi-square test). (**C-D**): Representative images of tissue sections labeled for vimentin (VIM) and keratin-8 (KRT8) (**C**) or Slug (SNAI2) and KRT8 (**D**) were taken using a confocal microscope. The average number of Slug-positive cells per field of view (**E**) or the relative KRT8-positive tumor area (**F**) were quantified (n=8 tumors from 2 independent experiments; unpaired t-test). (**G-H**): Representative images of tumor sections labeled for αSMA (ACTA2; **G**; n=5 tumors) or ITGA6 and KRT8 (**H**; nshCTRL = 3; nshMYO10 = 2 tumors). White squares represent ROIs that are magnified. (**I-K**): shCTRLGFP + shMYO10 or shMYO10GFP + shCTRL DCIS.com cells were xenografted in NOD.scid mice in 1:1 ratio. After 25 to 35 days, the resulting xenografts were imaged by intravital tile scan imaging (n = 2) (**I**) or dissected, sectioned, and imaged using a spinning-disk confocal microscope (20x objective) (**J**). The percentage of GFP-positive cells at the edge of DCIS acini was then scored using Fiji, and results displayed as Tukey box plots (**K**) (n = 4 tumors per condition; fields of view analyzed: shCTRLGFP + shMYO10, 114; shMYO10GFP + shCTRL,103; Mann-Whitney test). Scale bars: A, C, D, H: 50 μm; G, I, J: 100 μm.
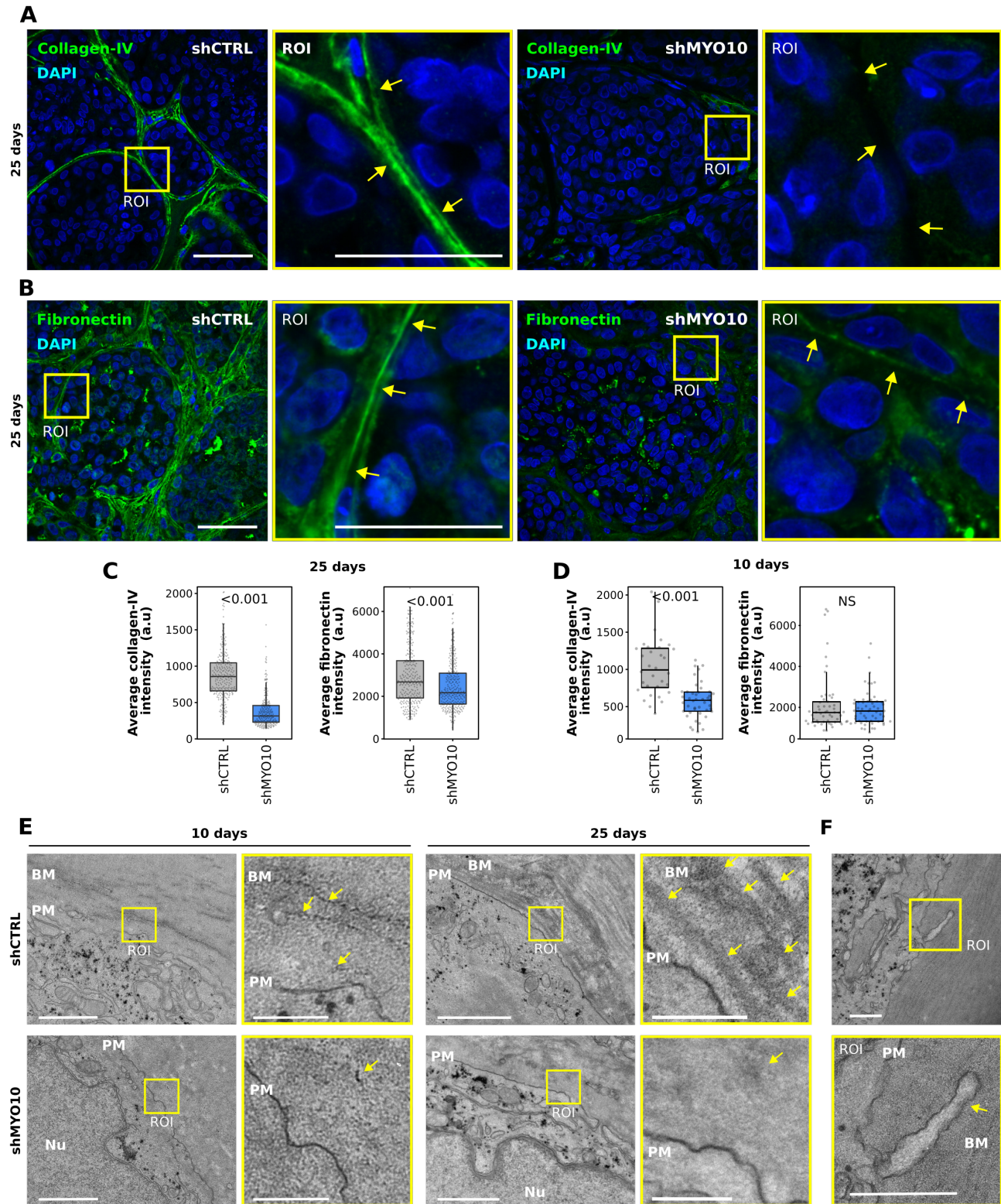
Fig. 3. MYO10 contributes to basement membrane integrity *in vivo*. (**A-D**): Tissue section of shCTRL and shMYO10 DCIS-like xenografts at day 25 (**A-C**) and day 10 (**D**) were stained for DAPI and collagen IV or fibronectin and imaged using a spinning-disk confocal microscope (63x objective). (**A-B**): Representative fields of view of day 25 DCIS-like xenografts are displayed. Scale bars: (main) 50 μm; (inset) 25 μm. (**C-D**): The average integrated density of collagen IV and fibronectin staining around the DCIS acini was measured using Fiji. The results are displayed as box plots (Day 25 xenografts, n > 233 DCIS acini from 5 tumors per condition; Day 10 xenografts, n > 32 DCIS acini from 4 tumors per condition; randomization test). (**E**): Day 10 and day 25 shCTRL and shMYO10 DCIS-like xenografts were imaged using electron microscopy to visualize the BM surrounding the DCIS acini. Representative fields of view are displayed (25-day-old xenografts, three biological repeats; ten-day-old xenografts, four biological repeats). Scale bars: (main) 1 μm; (inset) 250 nm. (**F**): Day 25 shCTRL DCIS-like xenografts were imaged using electron microscopy to visualize the protrusions surrounding the DCIS acini. Scale bars: (main) 500 nm; (inset) 500 nm. For all panels, p-values were determined using a randomization test. NS indicates no statistical difference between the mean values of the highlighted condition and the control. PM: plasma membrane; Nu: nucleus.
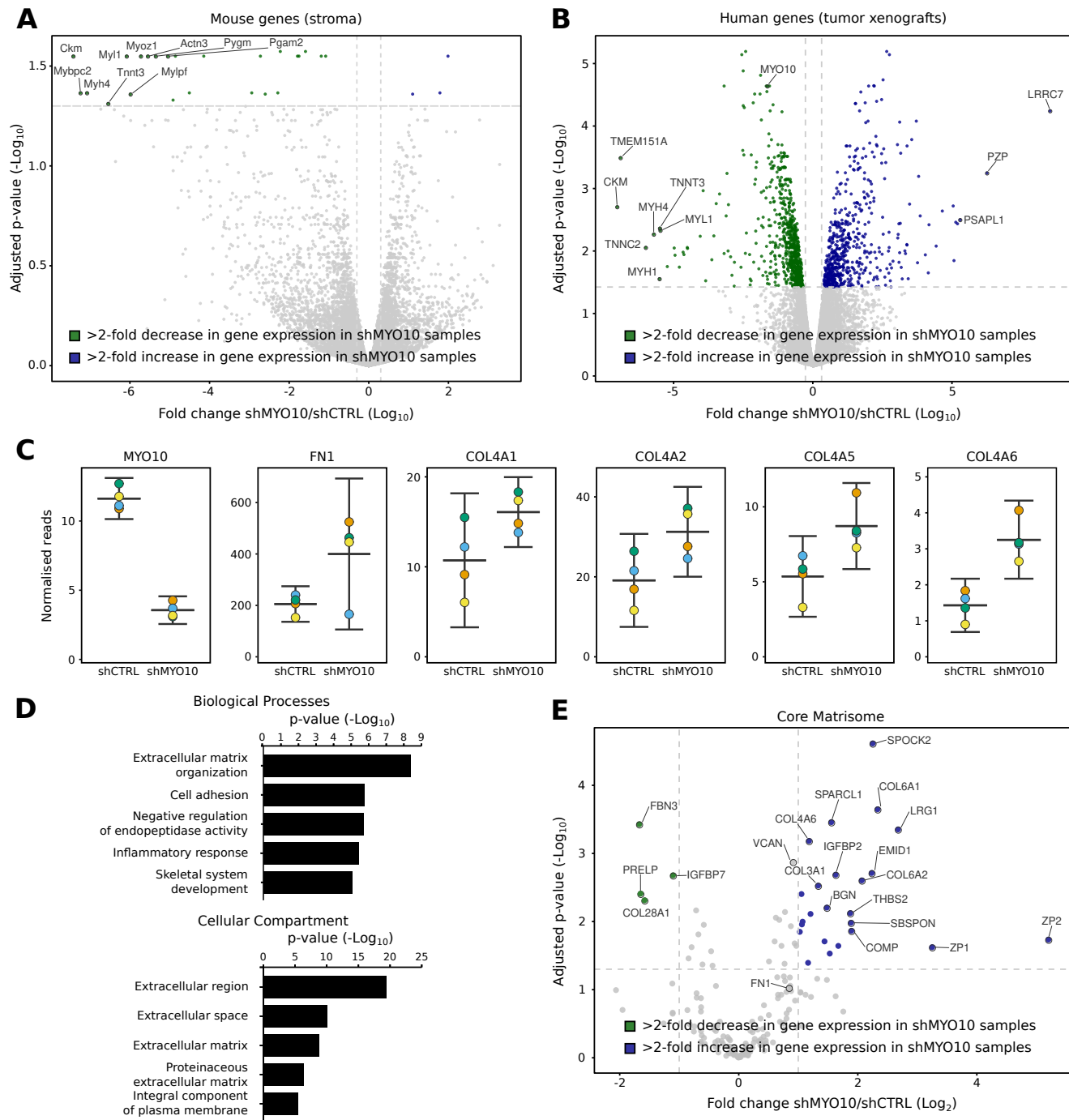
Fig. 4. MYO10 depletion drives the expression of ECM genes by cancer cells. (**A-E**): 25-day-old shCTRL and shMYO10 DCIS-like xenografts were dissected and their RNA sequenced. The expression levels of the mouse genes (tumor stroma) and of the human genes (tumor) were analyzed separately (**Table S1**, see methods for details, four different mice per condition). (**A-B**) The overall gene expression changes in the stroma (**A**) or the tumors (**B**) upon MYO10 silencing are displayed as volcano plots. Genes with at least a two-fold increase in their expression levels upon MYO10 silencing are highlighted in blue, while genes with at least a two-fold decrease in their expression levels upon MYO10 silencing are highlighted in green. The most affected genes and MYO10 are annotated. (**C**): The expression levels of MYO10 and selected ECM genes FN1, COL4A1, COL4A2, COL4A5, and COL4A6 in 25-day-old shCTRL and shMYO10 DCIS-like xenografts were measured by RNAseq and displayed as SuperPlots. (**D**): Gene ontology-based functional annotation analyses of human genes overexpressed in shMYO10 tumors (Biological Process and Cellular Compartment) were performed using DAVID (Huang et al., 2009). The top five categories (based on their adjusted p-values) are displayed. (**E**): Volcano plots highlighting the changes in core Matrisome gene expression upon MYO10 silencing (as defined by the Matrisome project).

were particularly obvious on the top and at the bottom of the spheroids (Fig. 5A and S7A). This was also seen while imaging spheroids live, indicating that this is not a fixation artifact (Video 6). Silencing MYO10 decreased filopodia density and resulted in a much weaker accumulation of ECM molecules at the edges of spheroids (Fig. 5B and 5C), indicating that MYO10-induced protrusions may contribute to ECM assembly in 3D.

MYO10 contributes to cell protrusions at the boundary of in situ tumor xenografts in vivo. Intrigued by the putative functional role of MYO10 protrusions in ECM assembly, we turned to live ex-vivo imaging of ECM-embedded tumors. Day 25 xenografts were dissected, embedded in a collagen gel, and imaged at high resolution. With lifeact-mRFP, we observed cells at the border of in situ tumors extending protrusions that interacted with the surrounding ECM (Fig. 6A-B, and Video 7). Notably, while very frequent in shCTRL cells, these protrusions were primarily absent in shMYO10 xenografts (Fig. 6C-D, and Video 8-9). These data indicate that MYO10 contributes to the generation of ECM-probing protrusions at the tumor border, reminiscent of the protruding filopodia detected in the 3D spheroids (Fig. 5A). It is important to note that the protrusions observed here are much bigger than individual filopodia and are more similar to pseudopods.

To assess how shCTRL and shMYO10 cells behave *in vivo*, we utilized two-photon intravital imaging (Fig. 6E). Although imaging of individual protrusions was beyond the image resolution with intravital microscopy, we investigated tumor cell motility. To enable single-cell tracking in the in vivo context, we mixed GFP-positive shCTRL or shMYO10 cells with non-GFP cells before injecting them into mice (see Methods for details). All xenografted cells also expressed lifeact-RFP. In agreement with our ex-vivo imaging (Fig. 6A-D) and 2D *in vitro* studies (Fig. 1 and Fig. S3), individual MYO10-depleted cells demonstrated reduced motility and active invasion in vivo compared to shCTRL cells (Fig. 6E and Video 10). Altogether, our data indicate that MYO10 contributes to the protrusive activity of DCIS.com cells *in vivo*, which correlates with defects in BM membrane assembly *in vivo* and *in vitro*.

Discussion

Here we set out to study the role of MYO10 in the transition of in-situ tumors to invasive carcinoma using a xenograft model that recapitulates key aspects of human breast cancer progression. We report that loss of MYO10 expression in breast cancer cells decreases filopodia formation in cells and spheroids *in vitro* and cell protrusions in tumors ex-vivo. DCIS-like xenografts with reduced MYO10 expression displayed defects in their basement membrane organization and increased dispersal of basal-like cells to the surrounding stroma. As MYO10-depleted xenografts produce more ECM mRNA than CTRL xenografts, and MYO10 promotes ECM deposition in 3D spheroid cultures, we propose a model by which tumor cell protrusive activity, induced by

MYO10, contributes to ECM deposition and basement membrane assembly at the tumor-stroma interface.

Filopodia are structurally related but functionally distinct from invadopodia (Jacquemet et al., 2015). Previous work indicated that invadopodia are involved in the degradation of BM, an event that is required for cancer cell dissemination in the surrounding stroma. Here we identified another functional difference between filopodia and invadopodia as we found that filopodia driven by MYO10 contribute to BM assembly. In particular, using high-resolution fixed and live imaging of 3D spheroids, we observed that ECM molecules are deposited at the base of filopodia. Our observations are consistent with a growing body of evidence of filopodia-like protrusions directly contributing to ECM remodeling in 3D and *in vivo* (Sato et al., 2017; Summerbell et al., 2020; Malandrino et al., 2019) and a report of leader cells in collectively migrating cell sheets remodeling fibronectin in the shafts of MYO10-positive filopodia (Summerbell et al., 2020). While the precise mechanism(s) by which filopodia remodel ECM remains to be determined, filopodia can assemble adhesive structures capable of interacting with different ECM molecules (Jacquemet et al., 2019; Miihkinen et al., 2021; Albuschies and Vogel, 2013). Filopodia can also exert forces on the underlying substrate, contributing to the remodeling process (Bornschlögl et al., 2013; Cojoc et al., 2007; Leijnse et al., 2015; Brockman et al., 2020). While such a mechanism can easily explain how filopodia-like protrusion can remodel fibronectin (Summerbell et al., 2020; Sato et al., 2017), a process known to require mechanical input from cells (Singh et al., 2010), it is more surprising that filopodia also contribute to the remodeling of BMs as these structures are typically thought to self-assemble (Jayadev and Sherwood, 2017). Future work will investigate how filopodia protrusions promote BM assembly.

To invade the surrounding tissues, tumor cells must cross the BM. In this context, BMs are typically viewed as stable barriers that inhibit cancer dissemination. However, recent evidence also suggests that BMs can be very dynamic structures that undergo fast and constant remodeling (Keeley et al., 2020). While, to the best of our knowledge, BM turnover has yet to be observed in tumors, the results presented here would support its existence. Indeed, we propose a model whereby cancer cells contribute to both the production and the assembly of the ECM. Previous work, using proteomic studies, also concluded that a large fraction of the ECM in the breast tumor stroma is produced by the cancer cells themselves (Naba et al., 2014; Kozma et al., 2021; Sflomos et al., 2021, 1). Interestingly, tumors lacking MYO10 not only have deficient BM but also have higher ECM gene expression. Therefore, it is tempting to speculate that a compensation mechanism(s) favors ECM production when ECM assembly is deficient.

MYO10 is frequently overexpressed in breast cancer, where its expression correlates with poor prognosis and mutant p53 expression (Arjonen et al., 2014; Cao et al., 2014). MYO10 silencing decreases cancer cell invasion and metastases of aggressive breast cancer cells *in vitro* and *in vivo* (Ar-
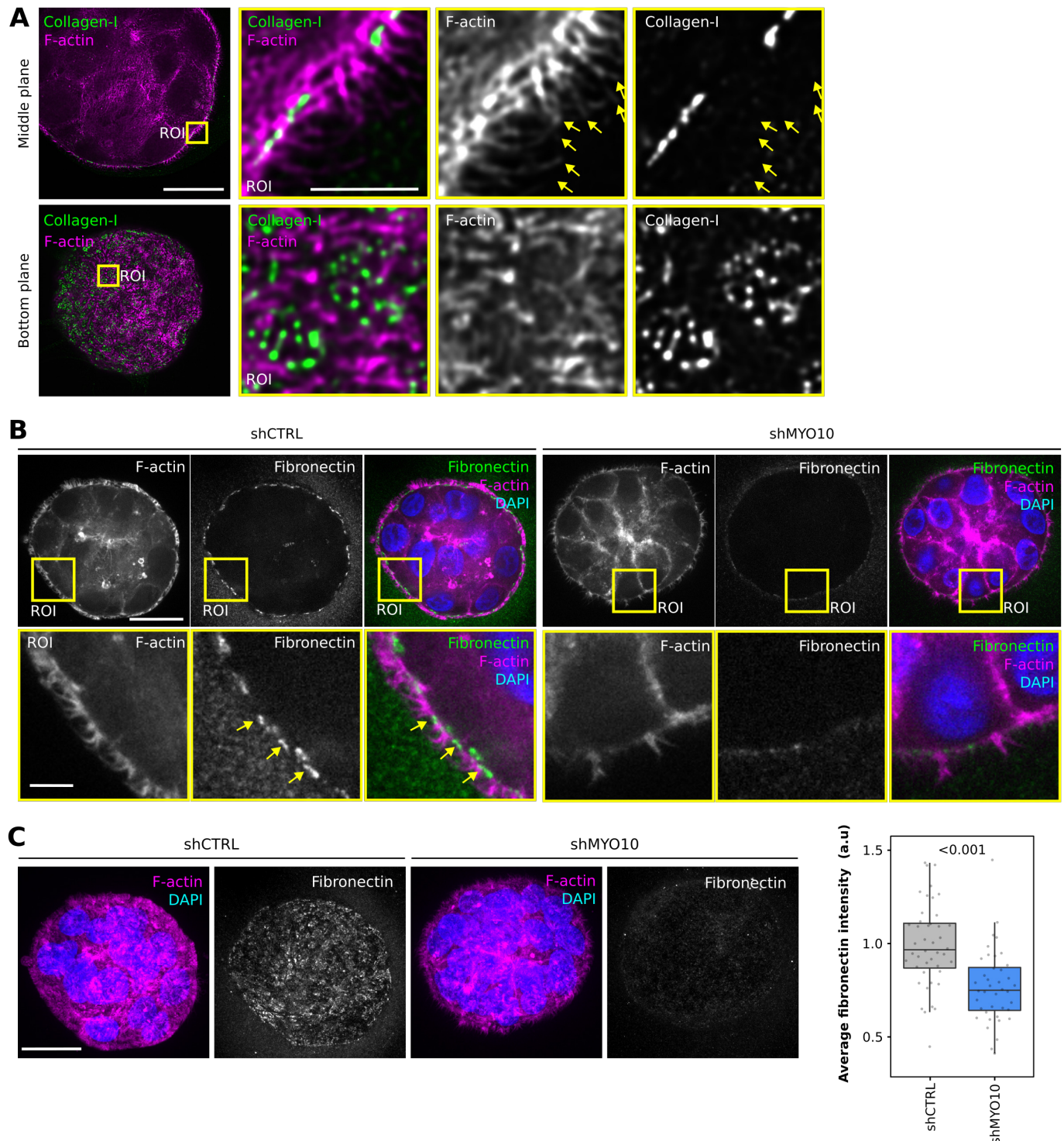
Fig. 5. MYO10 modulates ECM assembly in 3D spheroids. (**A**): DCIS.com cells were seeded as single cells in Matrigel. They were allowed to form spheroids for three days in the presence of fluorescently labeled collagen I. Samples were fixed and imaged using a spinning-disk confocal microscope and processed using eSRRF to perform fluctuation-based super-resolution microscopy. Representative fields of view highlighting the spheroids' middle and bottom planes are displayed. Scale bars: (main) 25 μm; (inset) 5 μm. (**B-C**): shCTRL and shMYO10 DCIS.com cells were allowed to form spheroids as in (**A**) in the presence of fluorescently labeled fibronectin and imaged using a spinning-disk confocal microscope (63x objective). Representative fields of view highlight the spheroids' middle planes (**B**) and SUM projections (**C**). Scale bars: (main) 25 μm; (inset) 5 μm. From the SUM projections, the average fibronectin intensity per spheroid was quantified using Fiji (n = 4 biological repeats; shCTRL, n = 44 spheroids; shMYO10, n = 40 spheroids; randomization test). Yellow squares indicate ROIs that are magnified.
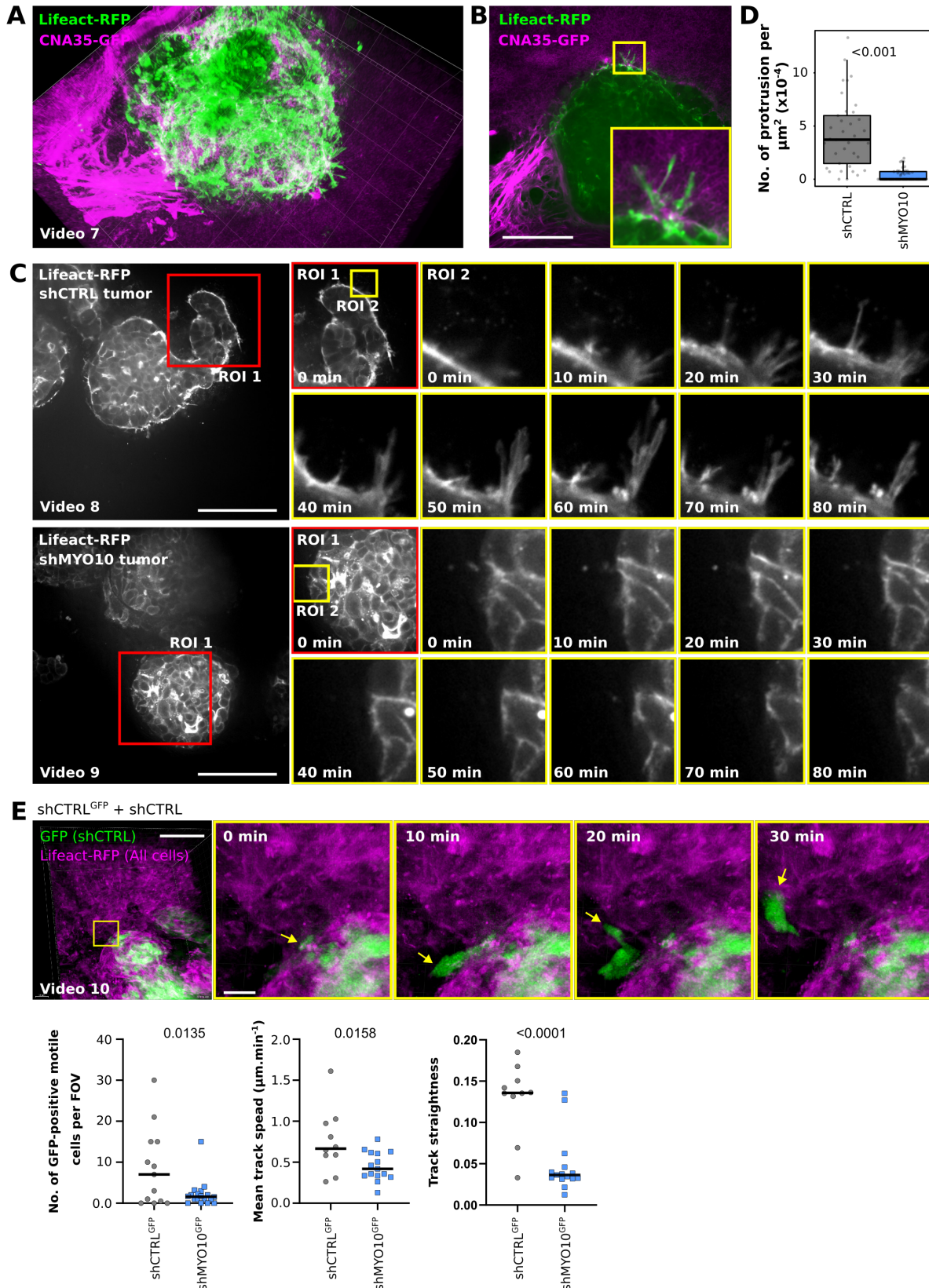
Fig. 6. MYO10 promotes cancer cell protrusion dynamics in DCIS-like xenografts. (**A-D**): Twenty-five-day-old DCIS-like xenografts were imaged live ex-vivo using a spinning-disk confocal microscope (40x objective, ORCA camera). Scale bars: (main) 100 µm. (**A-B**): shCTRL xenografts were incubated with the fibrillar collagen probe CNA35-GFP before imaging. A 3D reconstruction (**A**, see also Video 7) and a single Z plane (**B**) of a representative field of view is displayed. (**C-D**): shCTRL and shMYO10 xenografts were imaged live over an extended time. (**C**): Representative fields of view are shown (see also Videos 8-9). (**D**): From these images, the number of protruding cells was quantified (n > 38 fields of view; 3 independent experiments; randomization test). (**E**): shCTRLGFP or shMYO10GFP DCIS.com cells were injected subcutaneously (s.c. tumors) or orthotopically (o.t. tumors) with non-GFP cells in immunocompromised mice. Intravital imaging of tumors with mammary imaging window (o.t. tumors) or skin flap (s.c. tumors) was conducted 25-35 days post-tumor inoculation (see also Video 10). All visibly motile GFP-positive cells were tracked manually in three dimensions using the Imaris software, and the number of motile cells per field of view and mean track speed and track straightness (displacement/length of track) per cell were quantified (n = 4 shCTRL-GFP tumors with 2-4 FOVs per tumor; and n = 6 shMYO10-GFP tumors with 1-5 FOVs per tumor; t-test). Scale bars: (main) 100 µm (inset) 15 µm. FOV: field of view.

Peuhu, Jacquemet *et al.* | Myosin-X-dependent basement membranes limit breast cancer invasion

jonen et al., 2014), and MYO10 contributes to the invasion of other aggressive cancers, including melanoma and glioblastoma (Tokuo et al., 2018; Kenchappa et al., 2020). In line with these previous studies, we found that targeting MYO10 expression leads to reduced cell migration *in vitro* and *in vivo*. However, our results also implicate a role for MYO10 in regulating BM, an important structure known to limit cancer progression. While we could not address the metastatic progression in the DCIS xenograft model tested here, defects in BM assembly may accelerate metastasis in other contexts. Therefore, the possible anti- and pro-invasive functions of MYO10 should be carefully considered when therapeutic targeting of this protein is attempted. Targeting tumor cells' ability to remodel their own ECM may also offer therapeutic opportunities as ECM niches often cause dormancy and treatment resistance (Shibue et al., 2012; Barkan et al., 2010). Future work will be required to generalize the findings using additional MYO10 depletion strategies and other experimental models and investigate if filopodia targeting strategies may promote breast tumor clearance when combined with classical therapeutics, as shown for glioblastoma (Kenchappa et al., 2020).

Material and methods.

Cell lines. MCF10 DCIS.COM (DCIS.COM) lifeact-RFP cells were cultured in a 1:1 mix of DMEM (Merck) and F12 (Merck) supplemented with 5% horse serum (GIBCO BRL, Cat Number: 16050-122), 20 ng/ml human EGF (Merck, Cat Number: E9644), 0.5 mg/ml hydrocortisone (Merck, Cat Number: H0888-1G), 100 ng/ml cholera toxin (Merck, Cat Number: C8052-1MG), 10 µg/ml insulin (Merck, Cat Number: I9278-5ML), and 1% (vol/vol) penicillin/streptomycin (Merck, Cat Number: P0781- 100ML). The DCIS.COM lifeact-RFP cells were generated using lentiviruses, produced using pCDH-lifeAct mRFP, psPAX2, and pMD2.G constructs, as described previously (Jacquemet et al., 2017). The DCIS.COM lifeact-RFP shCTRL #s, shMYO10 #3 and shMYO10 #4 cell lines were generated using lentiviruses particles containing a non-target control shRNA (Merck, Cat Number: SHC016V-1EA) or shRNA targeting human MYO10 respectively (shMYO10 #3, TRCN0000123087; shMYO10 #4, TRCN0000123088). Transduced cells were selected using normal media supplemented with 2 µg.ml-1 of puromycin. DCIS.COM lifeact-RFP shCTRL and shMYO10 lines were generated from single-cell clones obtained from the DCIS.COM lifeact-RFP shMYO10 3 and shMYO10 4 cell lines. Four single-cell clones with normal MYO10 levels were pooled to create the shCTRL line, and four single-cell clones with very low MYO10 levels were pooled to create the shMYO10 line. The DCIS.COM lifeact-RFP shCTRL and shMYO10 GFP lines were generated using lentivirus particles containing GFP. Positive cells were sorted using a BD FACSaria II cell sorter (Becton Dickinson) with a gating strategy to obtain medium expression.

Antibodies and other reagents. Antibodies used in this studies were anti-Collagen IV (Abcam, Cat Number:

ab19808), anti-Fibronectin (FN, Merck, Cat Number: F3648), anti-MYO10 (Novus Biologicals, Cat Number: 22430002), anti-GFP (Abcam, Cat Number: Ab290), anti-alpha-smooth muscle actin (αSMA, clone 1A4, Merck, Cat Number: A2547), anti-Slug (clone C19G7, Cell Signalling Technology, Cat Number: 9585), anti-Vimentin (Clone V9, Santa Cruz, Cat Number: sc-6260), anti-Cleaved caspase-3 (Asp175, clone 5A1E, Cell Signalling Technology Cat Number: 9664), anti-BrdU (clone BU1/75 ICR1, Santa Cruz, Cat Number: sc-56258). The RFP-Booster Atto594 was provided by Chromotek (Cat Number: rb2AF568). Sir-DNA (SiR-Hoechst) (Lukinavičius et al., 2015) was provided by Tetubio (Cat Number: SC007). Growth factor reduced Matrigel was purchased from BD Biosciences (Cat Number: 354230). PureCol EZ Gel (fibrillar collagen I, concentration 5 mg/ml) was provided by Advanced BioMatrix (Cat Number: 5074). FITC-collagen was provided by Merk (type I collagen from bovine skin, Cat Number: C4361).

Generation of in situ tumor xenografts. For xenografts, 1×10^5 DCIS.com cells were resuspended in 100 µl of a mixture of 50% Matrigel (diluted in PBS) before being injected subcutaneously in the flank or orthotopically in the abdominal mammary gland of 6-7 -week-old virgin female NOD.scid mice (Envigo). Tumor growth was measured with a caliper 1-2 times per week. Mice were sacrificed 10 or 25 days post-injection (as indicated), and the tumors were dissected. For detecting tumor cell proliferation, BrdU Labelling Reagent (Life Technologies) was injected intraperitoneally according to the manufacturer's instructions (10 µl/g of mouse weight) 2 hours before sacrifice. The National Animal Experiment Board authorized all animal studies, and per The Finnish Act on Animal Experimentation (Animal license number ESAVI-9339-04.10.07-2016; Netherlands Cancer Institute NVWA license number 30100, Project number AVD301002015125).

Human tissues. Human breast tissue samples were obtained by breast cancer surgery at the Department of Plastic and General Surgery at Turku University Hospital (Turku, Finland) with approval from the Ethics Committee of the Hospital District of Southwestern Finland and written consent from the patients (§279, 9/2001). Human normal breast and breast cancer tissues were collected at Turku University Hospital (Ethical permit 23/1801/2018). Paired samples from breast tumors and surrounding peritumoral or contralateral normal breast tissues of 5 breast cancer patients were excised and examined by a clinical pathologist and, subsequently, processed to formalin-fixed paraffin-embedded (FFPE) tissue sections with standard protocols.

RNA in situ hybridization. RNA in situ hybridization was performed on human FFPE breast tissue sections with RNAscope® 2.5 HD Detection kit (BROWN, cat no. 322300) (Advanced Cell Diagnostics) based on manufacturer's instructions using a probe targeting the region 1262–2318 in MYO10 mRNA (RNAscope® Probe - Hs-MYO10-full, cat no. 440691). For negative and positive

controls RNAscope® Negative Control Probe – DapB (cat no. 310043) and RNAscope® Positive Control Probe - Hs-PPIB (cat no. 313901) were used, respectively (Advanced Cell Diagnostics). Nuclei were labeled with hematoxylin, and samples were mounted in DPX new (Merck). Samples were imaged with a Panoramic Slide Scanner (3DHistech).

Histology and immunohistochemistry. Formalin-fixed paraffin-embedded mouse xenograft tissues were sectioned and HE-labelled with standard procedures. Xenograft histology was scored blindly (in situ tumor/ in situ tumor with disorganized areas or partial invasion/ tumor with invasion). Immunohistochemistry was performed with standard protocols on deparaffinized sections after heat mediated antigen retrieval in Universal buffer (Retriever 2100, Aptum Bio) with antibodies against KRT8 (clone Troma I, Hybridoma Bank, 1:2000), alpha-smooth muscle actin (αSMA, clone 1A4, Merck, 1:1000), Col IV (ab19808, Abcam, 1:400), FN (F3648, Merck, 1:400), Slug (clone (C19G7, Cell Signalling Technology, 1:100), Vimentin (Clone V9, Santa Cruz, 1:200), Cleaved caspase-3 (Asp175, clone 5A1E, Cell Signalling Technology, 1:500), human mitochondria (clone 113-1, Merck Millipore, 1:100), and BrdU (clone BU1/75 ICR1, Santa Cruz, 1:300). All samples were stained with DAPI (4,6-diamidino-2-phenylindole, dihydrochloride; Life Technologies), mounted in Mowiol containing DABCO® (Merck) antifade reagent, and imaged with spinning-disk microscopy.

The percentage of GFP-positive cells at the edges of tumor acini was analyzed using Fiji (Schindelin et al., 2012). For each set of samples, four images were acquired: cancer cell marker (human mitochondria), ECM marker (Collagen IV), nuclei (DAPI), and GFP. The edge of tumor acini and its coordinates were first defined using the cancer cell and ECM markers. Then each cell was identified using the DAPI label, and its distance to the closest edge of tumor acini was calculated with R software. Using this information, cells were classified as edge cells (< than 10 μm distance) or not edge cells (> than 10 μm distance). Finally, the GFP channel was used to separate the GFP-positive cells from GFP-negative and quantify the percentage of GFP-positive cells at the edge of tumor acini.

Light microscopy setup. The spinning-disk confocal microscope used was a Marianas spinning-disk imaging system with a Yokogawa CSU-W1 scanning unit on an inverted Zeiss Axio Observer Z1 microscope controlled by SlideBook 6 (Intelligent Imaging Innovations, Inc.). Images were acquired using either an Orca Flash 4 sCMOS camera (chip size 2,048 × 2,048; Hamamatsu Photonics) or an Evolve 512 EMCCD camera (chip size 512 × 512; Photometrics). Objectives used were a 20X air objective (NA 0.8, Plan-Apochromat, Zeiss), a 40x water (NA 1.1, LD C-Apochromat, Zeiss), a 63× oil (NA 1.4, Plan-Apochromat, M27 with DIC III Prism, Zeiss) and a 100x oil (NA 1.4 oil, Plan-Apochromat, M27) objective. The confocal microscope used was a laser scanning confocal microscope LSM880 (Zeiss) equipped with an Airyscan detector (Carl Zeiss) and a 40x oil (NA 1.4) objective. The

microscope was controlled using Zen Black (2.3), and the Airyscan was used in standard super-resolution mode.

Circular invasion assays. Cells were plated in one well of a two-well culture-insert (Ibidi, Cat Number: 80209) pre-inserted within a well of a μ-Slide 8 well (Ibidi, Cat Number: 80807). After 24 h, the culture-insert was removed, and a fibrillar collagen gel (PureCol EZ Gel) was cast. The gel was allowed to polymerize for 30 min at 37°C before normal media was added on top. Cells were left to invade for two days before fixation or live imaging. To analyze filopodia properties, fixed samples were stained with phalloidin-488 and imaged using a spinning-disk confocal microscope (100x objective). Filopodia density and length were then automatically analyzed using the FiloQuant implemented in Fiji (Schindelin et al., 2012; Jacquemet et al., 2017). To analyze the effect of MYO10 silencing on cell migration, shC-TRL, and shMYO10 cells were incubated for 2 h with 0.5 μM SiR-DNA (SiR-Hoechst, Tetu-bio, Cat Number: SC007) before being imaged live for 14 h using a spinning-disk confocal microscope (20x objective, 1 picture every 10 min). Nuclei were automatically detected using the deep learning algorithm StarDist implemented in the ZeroCostDL4Mic platform and tracked using TrackMate (Ershov et al., 2021; Fazeli et al., 2020; Tinevez et al., 2017; Schmidt et al., 2018; von Chamier et al., 2021). This custom StarDist model was trained for 100 epochs on 72 paired image patches (image dimensions: 1024x1024, patch size: 1024x1024) with a batch size of 2 and a mae loss function, using the StarDist 2D Zero-CostDL4Mic notebook (v1.12.2). The StarDist "Versatile fluorescent nuclei" model was used as a training starting point. The training was accelerated using a Tesla P100. This model generated excellent segmentation results on our test dataset (average Intersection over union > 0.96; average F1 score > 0.96) (Laine et al., 2021). The StarDist model and the training dataset used are available for download on Zenodo (Guillaume Jacquemet, 2020). Cell tracks were further analyzed using the Motility Lab website Motility Lab website (Wortel et al., 2019). To analyze the effect of MYO10 silencing on cell protrusions, shCTRL and shMYO10 cells were imaged live for a few hours using a spinning-disk confocal microscope (100x objective, 1 picture every 3 min). Images were then processed using Fiji (Schindelin et al., 2012).

To perform migration competition assays, GFP positive and negative DCIS.com cell lines were mixed with a 50/50% ratio before being plated in a circular invasion assay. Cells were imaged live for 16 h using a spinning-disk confocal microscope (20x objective, 1 picture every 10 min). For each time point, the migration edges and the GFP-positive cells were automatically segmented and the percentage of the leading edge covered by the GFP-positive cell was then calculated.

ECM remodeling. To form spheroids, DCIS.com cells were seeded as single cells, in standard growth media, at very low density (3,000 cells per well) on growth factor reduced (GFR) Matrigel-coated glass-bottom dishes (coverslip No. 0; MatTek). After 12 h, the medium was replaced by a nor-

mal growth medium supplemented with 2% (vol/vol) GFR Matrigel and 10 µg.ml-1 of a fluorescently labeled ECM molecule. After three days, spheroids were imaged live or fixed with 4% PFA for 10 min at room temperature.

To allow for fluctuation-based super-resolution (Jacquemet et al., 2020) using NanoJ-eSRRF, fields of view of interest were imaged 100 times using a spinning-disk confocal microscope (63x objective). NanoJ-eSRRF is the newest implementation of NanoJ-SRRF (Gustafsson et al., 2016; Stubb et al., 2020) within the ImageJ software (Schneider et al., 2012). One hundred frames were used for the reconstruction. The parameter sweep option and SQUIRREL analyzes (Culley et al., 2018), integrated within eSRRF, were used to define the optimal reconstruction parameters. NanoJ-eSRRF was kindly provided by Romain Laine and Ricardo Henriques and is available from them upon request.

To quantify the amount of ECM remodeling occurring at the surface of DCIS.com spheroids, 3D stacks were acquired using a spinning-disk confocal microscope (step size 0.5 µm). SUM projections were performed, and the integrated intensity was quantified for each spheroid using Fiji (Schindelin et al., 2012). Spheroids were imaged live using a spinning-disk confocal microscope. Videos were denoised using the deep Learning algorithm Deconoising (Goncharova et al., 2020) implemented within ZeroCostDL4Mic (von Chamier et al., 2021). The DecoNoising models were trained for 200 epochs directly on the images to denoise using a patch size of 80x 80 pixels, a batch size of 4, and a virtual batch size of 20, using the DecoNoising 2D ZeroCostDL4Mic notebook (v1.12). The training was accelerated using a Tesla P100 GPU, and data augmentation was enabled.

ex-vivo imaging of DCIS xenografts. To perform ex-vivo imaging, twenty-five days old DCIS-like xenografts were dissected, incubated with fibrillar collagen probe CNA35-GFP (when indicated, produced in-house, (Aper et al., 2014)), deposited in a glass-bottom dish (coverslip No. 0; MatTek), and embedded in a collagen-I gel (Advanced BioMatrix, Cat Number: 5074). The gel was then allowed to polymerize at 37 C for 15 min, and the DCIS.com culture medium was added on top. Xenografts were then imaged live using a spinning-disk confocal microscope (40X objective, imaging starting less than 1 h post dissection). Images were processed using Fiji. 3D visualizations were performed using Imaris (Oxford Instruments) and Arivis Vision4D (Arivis).

Surgical procedures and intravital imaging. Tumor-bearing mice were anesthetized with a 1.5%-2% isoflurane/air mixture. To visualize the subcutaneous tumors, a skin flap surgery was performed. The area around the tumor was shaved, disinfected, and a vertical midline incision was made through the skin, followed by two horizontal incisions anterior and posterior of the tumor area. The skin was detached from the underlying tissues and peritoneum by blunt dissection/gentle pulling with a curved instrument. The mouse was transferred to a custom-made imaging box connected to an isoflurane vaporizer. The mouse was placed on top of a metal

inlay with a rectangular opening covered with a coverglass. The skin flap was opened, and the tumor area was placed on the coverglass. A sterile gauze soaked in preheated PBS was placed on top of the skin flap to maintain hydration, and parafilm was used to cover the skin flap and create a humidified chamber. To visualize the orthotopic tumors, implantation of an optical imaging window was carried out as described by (Messal et al., 2021). In short, the tumor area was shaved and disinfected, and a 10-15mm incision was made above the tumor. The skin was loosened from the tumor tissue by blunt dissection, and a non-absorbable silk suture was placed in loops around the incision. A sterilized titanium mammary imaging window with a fixed glass coverslip was inserted and secured in the skin with the purse-string suture. After window implantation, the mouse was transferred to a custom-designed imaging box on top of an inlay designed with a hole to secure the imaging window. During time-lapse imaging, the mouse received nutrition through a subcutaneously placed flexible needle (100 µl/hr, Nutriflex (R) special 70/240). Intravital imaging was conducted with an inverted Leica SP8 DIVE microscope (Leica Microsystems) equipped with four tunable hybrid detectors, a MaiTai eHP DeepSee laser (Spectra-Physics), and an InSight X3 laser (Spectra-Physics). For image acquisition, Leica Application Suite X (LAS X) was used.

All images were collected at 12 bit and acquired with a $25 \times$ water immersion objective with a free working distance of 2.40 mm (HC FLUOTAR L 25x/0.95 W VISIR 0.17). GFP and mRFP were excited with 925 nm and 960 nm and detected between 490-550 nm and 580-650 nm, respectively. The second-harmonic generation signal was collected to visualize Collagen I. Whole-tumor areas were imaged by 3D tiles can imaging with a z-step size of 6µm. Timelapse imaging of regions of interest (XYZT) was performed at a 5- or 20-minute time interval for up to 12 hours. Imaged regions were stitched over time using Leica LASX software, and XYZ-drift corrections were performed using Huygens Object Stabilizer software (Scientific Volume Imaging). 3D renderings displayed in Video 4 and 5 were created using the LAS X 3D Visualization module. Motile cells were manually tracked using Imaris software (version 9.0, Oxford Instruments). The mean track speed and persistence were quantified along with the number of invasive (protruding/motile) GFP+ cells per FOV. Image sequences with high cell blebbing (apoptosis due to limited blood supply) were excluded.

RNA sequencing and analyses. Tumors were dissected 25 days after inoculation and stored in an RNAlater lysis buffer (Producer). RNA was extracted from tissue (ca <30mg/sample) collected to H_2O using the Qiagen RNeasy Plus Mini kit. The quality of the total RNA samples was ensured with Agilent Bioanalyzer 2100. Sample concentration was measured with Nanodrop ND-2000, Thermo Scientific. Total RNA samples were pure, intact and all samples had a similar quality. Bioanalyzer RIN values were > 9.4. The library preparation was started from 100 ng of total RNA.

Library preparation was done according to Illumina TruSeq® Stranded mRNA Sample Preparation Guide (part#

15031047). The high quality of the libraries was confirmed with Agilent Bioanalyzer 2100, and the concentrations of the libraries were quantified with Qubit® Fluorometric Quantitation, Life Technologies. Library quality was excellent, and all samples had similar quality (fragments in the range of 200-700 bp and the average size of the fragments 250-350 bp). The samples were normalized and pooled for the automated cluster preparation which was carried out with Illumina cBot station. The 8 libraries were pooled in one pool and run in one lane. The samples were sequenced with the Illumina HiSeq 3000 instrument. Paired-end sequencing with 2 x 75 bp read length was used with 8 + 8 bp dual index run. The technical quality of the HiSeq 3000 run was good, and the cluster amount was as expected. Greater than 75% of all bases above Q30 were requested. The typical yields are 260-310 x 106 paired-end or single-end reads per lane on HiSeq 3000, depending on the library type and quality. The base calling was performed using Illumina's standard bcl2fastq2 software, and automatic adapter trimming was used.

The quality of the sequencing reads was checked using the FastQC tool (v. 0.11.4). The reads were analyzed against both human and mouse references. First, the sequencing reads were separately aligned to human (UCSC hg38) and mouse (UCSC mm10) reference genomes, derived from the Illumina iGenomes resource, using STAR aligner (v. 2.5.2b) (Dobin et al., 2013). For mouse reference, the reads that also aligned to human reference were removed using XenofilteR (v. 0.99.0) (Kluin et al., 2018). Next, the uniquely aligned reads were associated with RefSeq gene models using Subread (v. 1.5.1) (Liao et al., 2014) for each organism. Normalization and statistical testing were carried out with R (v. 3.4.1) and Bioconductor (v. 3.6) (Gentleman et al., 2004), using edgeR (McCarthy et al., 2012) and Limma packages (Ritchie et al., 2015). In each comparison, genes with mean RPKM expression value below 0.125 in both sample groups were filtered out, and the normalized expression values were voom transformed before statistical testing. An absolute fold-change above two and a false discovery rate (FDR) smaller than 0.01 or 0.05 were required to select the differentially expressed genes.

Quantitative RT-PCR .   Total RNA extracted using the NucleoSpin RNA Kit (Macherey-Nagel) was reverse transcribed into cDNA using the high-capacity cDNA reverse transcription kit (Applied Biosystems) according to the manufacturer's instructions. The RT-PCR reactions were performed using pre-designed single tube TaqMan gene expression assays (GAPDH: Hs03929097_g1) and were analyzed with the 7900HT fast RT-PCR System (Applied Biosystems). Data were studied using RQ Manager Software (Applied Biosystems).

Electron microscopy.   The samples were fixed with 5% glutaraldehyde in s-collidine buffer, postfixed with 1% OsO4 containing 1.5% potassium ferrocyanide, dehydrated with ethanol, and embedded in 45359 Fluka Epoxy Embedding Medium kit. Thin sections were cut using an ultramicrotome to a thickness of 70 nm. The sections were stained using uranyl acetate and lead citrate. The sections were examined using a JEOL JEM-1400 Plus transmission electron microscope operated at 80 kV acceleration voltage.

Proliferation assay.   To monitor cell proliferation *in vitro*, cells were plated at low density in a well of a six-well plate and imaged using a live-cell microscopy incubator (IncuCyte ZOOM). Growth rates were calculated using the confluency method within the IncuCyte ZOOM software.

Spheroid growth assays.   Chamber slides (15-well, Ibidi) were coated with Matrigel, spun down at 300g for 10 min at 4C, and incubated at 37 C until the Matrigel solidified. Subsequently, shCTRL or shMYO10 DCIS.com cells were resuspended in 70% Matrigel/30% PureCol EZ Gel (Advanced Biomatrix) (500 cells/20µl/well). After 30 min in an incubator, 40µl of DCIS.com culture medium was added on top of solidified cultures. The medium was refreshed every 2-3 days, and cultures were fixed with 4% PFA in PBS (10min at RT) 7 days after seeding. Lifeact-RFP (Riedl et al., 2008) signal was imaged using a spinning-disk confocal microscope (10x/40x objective), and the area covered by each spheroid was segmented and quantified in Fiji (Schindelin et al., 2012).

Western blotting.   Protein extracts were separated under denaturing conditions by SDS–PAGE and transferred to nitrocellulose membranes. Membranes were blocked for one hour at room temperature with a blocking buffer (LI-COR Biosciences) and then incubated overnight at 4 °C with the appropriate primary antibody diluted in the blocking buffer. Membranes were washed with PBS and then incubated with the appropriate fluorophore-conjugated secondary antibody diluted 1:5,000 in a blocking buffer for 30 min. Membranes were washed in the dark and then scanned using an Odyssey infrared imaging system (LI-COR Biosciences).

Quantification and statistical analysis.   Randomization tests were performed using PlotsOfDifferences (Goedhart, 2019). Dot plots were generated using PlotsOfData (Postma and Goedhart, 2019), Volcano Plots were generated using VolcaNoseR (Goedhart and Luijsterburg, 2020), and SuperPlots were generated using SuperPlotsOfData (Goedhart, 2021; Lord et al., 2020). Other statistical tests were performed using GraphPad Prism software. The Student's t-test (unpaired, two-tailed) was used for normally distributed data. Non-parametric Mann–Whitney U-test was used when two non-normally distributed groups were compared. Fisher's exact test was used for the analysis of contingency tables. Data representation and n-numbers for each graph are indicated in figure legends.

Data and code availability .   The StarDist model used to track cells automatically is available on Zenodo (Guillaume Jacquemet, 2020). The RNA sequencing dataset generated here has been added to Gene Expression Omnibus (GEO) database repository (GSE166898). The authors declare that the rest of the data described in this manuscript are also available upon request.

AUTHOR CONTRIBUTIONS

Conceptualization, E.P., G.J., J.I.; Methodology, E.P., G.J., J.I., C. L.G.J. S.; Formal Analysis, E.P., G.J., C.L.G.J.S., A. I., C. G., S.K., A.L., L.L.E., M. G.; Investigation, E. P., G. J., C. L.G.J. S., I. P., K. T., M. G., P. B., I.P.; Writing – Original Draft, E.P., G.J., J.I.; Writing – Review and Editing, All authors; Visualization, E.P., G.J., J.I.; Supervision, E.P., G.J., J.I., L. L. E., J. v. R.; Funding Acquisition, E.P., G.J., J.I..

Bibliography

Albuschies, J., and V. Vogel. 2013. The role of filopodia in the recognition of nanotopographies. Sci. Rep. 3:1658. doi:10.1038/srep01658.

Aper, S.J.A., A.C.C. van Spreeuwel, M.C. van Turnhout, A.J. van der Linden, P.A. Pieters, N.L.L. van der Zon, S.L. de la Rambelje, C.V.C. Bouten, and M. Merkx. 2014. Colorful Protein-Based Fluorescent Probes for Collagen Imaging. PLOS ONE. 9:e114983. doi:10.1371/journal.pone.0114983.

Arjonen, A., R. Kaukonen, E. Mattila, P. Rouhi, G. Högnäs, H. Sihto, B.W. Miller, J.P. Morton, E. Bucher, P. Taimen, R. Virtakoivu, Y. Cao, O.J. Sansom, H. Joensuu, and J. Ivaska. 2014. Mutant p53-associated myosin-X upregulation promotes breast cancer invasion and metastasis. J. Clin. Invest. 124:1069–1082. doi:10.1172/JCI67280.

Barkan, D., L.H. El Touny, A.M. Michalowski, J.A. Smith, I. Chu, A.S. Davis, J.D. Webster, S. Hoover, R.M. Simpson, J. Gauldie, and J.E. Green. 2010. Metastatic growth from dormant cells induced by a col-I-enriched fibrotic environment. Cancer Res. 70:5706–5716. doi:10.1158/0008-5472.CAN-09-2356.

Bornschlögl, T., S. Romero, C.L. Vestergaard, J.-F. Joanny, G.T.V. Nhieu, and P. Bassereau. 2013. Filopodial retraction force is generated by cortical actin dynamics and controlled by reversible tethering at the tip. Proc. Natl. Acad. Sci. 110:18928–18933. doi:10.1073/pnas.1316572110.

Brockman, J.M., H. Su, A.T. Blanchard, Y. Duan, T. Meyer, M.E. Quach, R. Glazier, A. Bazrafshan, R.L. Bender, A.V. Kellner, H. Ogasawara, R. Ma, F. Schueder, B.G. Petrich, R. Jungmann, R. Li, A.L. Mattheyses, Y. Ke, and K. Salaita. 2020. Live-cell super-resolved PAINT imaging of piconewton cellular traction forces. Nat. Methods. 17:1018–1024. doi:10.1038/s41592-020-0929-2.

Cao, R., J. Chen, X. Zhang, Y. Zhai, X. Qing, W. Xing, L. Zhang, Y.S. Malik, H. Yu, and X. Zhu. 2014. Elevated expression of myosin X in tumours contributes to breast cancer aggressiveness and metastasis. Br. J. Cancer. 111:539–550. doi:10.1038/bjc.2014.298.

von Chamier, L., R.F. Laine, J. Jukkala, C. Spahn, D. Krentzel, E. Nehme, M. Lerche, S. Hernández-Pérez, P.K. Mattila, E. Karinou, S. Holden, A.C. Solak, A. Krull, T.-O. Buchholz, M.L. Jones, L.A. Royer, C. Leterrier, Y. Shechtman, F. Jug, M. Heilemann, G. Jacquemet, and R. Henriques. 2021. Democratising deep learning for microscopy with ZeroCostDL4Mic. Nat. Commun. 12:2276. doi:10.1038/s41467-021-22518-0.

Clark, A.G., and D.M. Vignjevic. 2015. Modes of cancer cell invasion and the role of the microenvironment. Curr. Opin. Cell Biol. 36:13–22. doi:10.1016/j.ceb.2015.06.004.

Cojoc, D., F. Difato, E. Ferrari, R.B. Shahapure, J. Laishram, M. Righi, E.M.D. Fabrizio, and V. Torre. 2007. Properties of the Force Exerted by Filopodia and Lamellipodia and the Involvement of Cytoskeletal Components. PLOS ONE. 2:e1072. doi:10.1371/journal.pone.0001072.

Culley, S., D. Albrecht, C. Jacobs, P.M. Pereira, C. Leterrier, J. Mercer, and R. Henriques. 2018. Quantitative mapping and minimization of super-resolution optical imaging artifacts. Nat. Methods. 15:263–266. doi:10.1038/nmeth.4605.

Dobin, A., C.A. Davis, F. Schlesinger, J. Drenkow, C. Zaleski, S. Jha, P. Batut, M. Chaisson, and T.R. Gingeras. 2013. STAR: ultrafast universal RNA-seq aligner. Bioinforma. Oxf. Engl. 29:15–21. doi:10.1093/bioinformatics/bts635.

Eddy, R.J., M.D. Weidmann, V.P. Sharma, and J.S. Condeelis. 2017. Tumor Cell Invadopodia: Invasive Protrusions that Orchestrate Metastasis. Trends Cell Biol. 27:595–607. doi:10.1016/j.tcb.2017.03.003.

Ershov, D., M.-S. Phan, J.W. Pylvänäinen, S.U. Rigaud, L.L. Blanc, A. Charles-Orszag, J.R.W. Conway, R.F. Laine, N.H. Roy, D. Bonazzi, G. Duménil, G. Jacquemet, and J.-Y. Tinevez. 2021. Bringing TrackMate into the era of machine-

learning and deep-learning.

Fazeli, E., N.H. Roy, G. Follain, R.F. Laine, L. von Chamier, P.E. Hänninen, J.E. Eriksson, J.-Y. Tinevez, and G. Jacquemet. 2020. Automated cell tracking using StarDist and TrackMate. F1000Research. 9:1279. doi:10.12688/f1000research.27019.1.

Ferlay, J., M. Colombet, I. Soerjomataram, T. Dyba, G. Randi, M. Bettio, A. Gavin, O. Visser, and F. Bray. 2018. Cancer incidence and mortality patterns in Europe: Estimates for 40 countries and 25 major cancers in 2018. Eur. J. Cancer Oxf. Engl. 1990. 103:356–387. doi:10.1016/j.ejca.2018.07.005.

Ferrari, R., G. Martin, O. Tagit, A. Guichard, A. Cambi, R. Voituriez, S. Vassilopoulos, and P. Chavrier. 2019. MT1-MMP directs force-producing proteolytic contacts that drive tumor cell invasion. Nat. Commun. 10:4886. doi:10.1038/s41467-019-12930-y.

Fierro-González, J.C., M.D. White, J.C. Silva, and N. Plachta. 2013. Cadherin-dependent filopodia control preimplantation embryo compaction. Nat. Cell Biol. 15:1424–1433. doi:10.1038/ncb2875.

Frittoli, E., A. Palamidessi, P. Marighetti, S. Confalonieri, F. Bianchi, C. Malinverno, G. Mazzarol, G. Viale, I. Martin-Padura, M. Garré, D. Parazzoli, V. Mattei, S. Cortellino, G. Bertalot, P.P. Di Fiore, and G. Scita. 2014. A RAB5/RAB4 recycling circuitry induces a proteolytic invasive program and promotes tumor dissemination. J. Cell Biol. 206:307–328. doi:10.1083/jcb.201403127.

Gentleman, R.C., V.J. Carey, D.M. Bates, B. Bolstad, M. Dettling, S. Dudoit, B. Ellis, L. Gautier, Y. Ge, J. Gentry, K. Hornik, T. Hothorn, W. Huber, S. Iacus, R. Irizarry, F. Leisch, C. Li, M. Maechler, A.J. Rossini, G. Sawitzki, C. Smith, G. Smyth, L. Tierney, J.Y. Yang, and J. Zhang. 2004. Bioconductor: open software development for computational biology and bioinformatics. Genome Biol. 5:R80. doi:10.1186/gb-2004-5-10-r80.

Glentis, A., P. Oertle, P. Mariani, A. Chikina, F. El Marjou, Y. Attieh, F. Zaccarini, M. Lae, D. Loew, F. Dingli, P. Sirven, M. Schoumacher, B.G. Gurchenkov, M. Plodinec, and D.M. Vignjevic. 2017. Cancer-associated fibroblasts induce metalloprotease-independent cancer cell invasion of the basement membrane. Nat. Commun. 8:924. doi:10.1038/s41467-017-00985-8.

Goedhart, J. 2019. PlotsOfDifferences – a web app for the quantitative comparison of unpaired data. bioRxiv. 578575. doi:10.1101/578575.

Goedhart, J. 2021. SuperPlotsOfData—a web app for the transparent display and quantitative comparison of continuous data from different conditions. Mol. Biol. Cell. 32:470–474. doi:10.1091/mbc.E20-09-0583.

Goedhart, J., and M.S. Luijsterburg. 2020. VolcaNoseR is a web app for creating, exploring, labeling and sharing volcano plots. Sci. Rep. 10:20560. doi:10.1038/s41598-020-76603-3. Goncharova, A.S., A. Honigmann, F. Jug, and A. Krull. 2020. Improving Blind Spot Denoising for Microscopy. ArXiv200808414 Cs Eess.

Guillaume Jacquemet. 2020. Combining StarDist and TrackMate example 1 - Breast cancer cell dataset. doi:10.5281/zenodo.4034976.

Gustafsson, N., S. Culley, G. Ashdown, D.M. Owen, P.M. Pereira, and R. Henriques. 2016. Fast live-cell conventional fluorophore nanoscopy with ImageJ through super-resolution radial fluctuations. Nat. Commun. 7:12471. doi:10.1038/ncomms12471.

Huang, D.W., B.T. Sherman, and R.A. Lempicki. 2009. Systematic and integrative analysis of large gene lists using DAVID bioinformatics resources. Nat. Protoc. 4:44–57. doi:10.1038/nprot.2008.211.

Huang, F.-K., S. Han, B. Xing, J. Huang, B. Liu, F. Bordeleau, C.A. Reinhart-King, J.J. Zhang, and X.-Y. Huang. 2015. Targeted inhibition of fascin function blocks tumour invasion and metastatic colonization. Nat. Commun. 6:7465. doi:10.1038/ncomms8465.

Jacquemet, G., A.F. Carisey, H. Hamidi, R. Henriques, and C. Leterrier. 2020. The cell biologist's guide to super-resolution microscopy. J. Cell Sci. 133. doi:10.1242/jcs.240713.

Jacquemet, G., D.M. Green, R.E. Bridgewater, A. von Kriegsheim, M.J. Humphries, J.C. Norman, and P.T. Caswell. 2013. RCP-driven α5β1 recycling suppresses Rac and promotes RhoA activity via the RacGAP1-IQGAP1 complex. J. Cell Biol. 202:917–935. doi:10.1083/jcb.201302041.

Jacquemet, G., H. Hamidi, and J. Ivaska. 2015. Filopodia in cell adhesion, 3D migration and cancer cell invasion. Curr. Opin. Cell Biol. 36:23–31.

Jacquemet, G., I. Paatero, A.F. Carisey, A. Padzik, J.S. Orange, H. Hamidi, and J. Ivaska. 2017. FiloQuant reveals increased filopodia density during breast cancer progression. J. Cell Biol. 216:3387–3403. doi:10.1083/jcb.201704045.

Jacquemet, G., A. Stubb, R. Saup, M. Miihkinen, E. Kremneva, H. Hamidi, and J. Ivaska. 2019. Filopodome Mapping Identifies p130Cas as a Mechanosensitive Regulator of Filopodia Stability. Curr. Biol. 29:202-216.e7. doi:10.1016/j.cub.2018.11.053.

Jayadev, R., and D.R. Sherwood. 2017. Basement membranes. Curr. Biol. 27:R207–R211. doi:10.1016/j.cub.2017.02.006.

Keeley, D.P., E. Hastie, R. Jayadev, L.C. Kelley, Q. Chi, S.G. Payne, J.L. Jeger, B.D. Hoffman, and D.R. Sherwood. 2020. Comprehensive Endogenous Tagging of Basement Membrane Components Reveals Dynamic Movement within the Matrix Scaffolding. Dev. Cell. 54:60-74.e7. doi:10.1016/j.devcel.2020.05.022.

Kenchappa, R.S., P. Mistriotis, E. Wisniewski, S. Bhattacharya, T. Kulkarni, R. West, A. Luu, M. Conlon, E. Heimsath, J.F. Crish, H.S. Picariello, A. Dovas, N. Zarco, M. Lara-Velazquez, A. Quiñones-Hinojosa, J.A. Hammer, D. Mukhopadhyay, R.E. Cheney, K. Konstantopoulos, P. Canoll, and S.S. Rosenfeld. 2020. Myosin 10 Regulates Invasion, Mitosis, and Metabolic Signaling in Glioblastoma. iScience. 23:101802. doi:10.1016/j.isci.2020.101802.

Kluin, R.J.C., K. Kemper, T. Kuilman, J.R. de Ruiter, V. Iyer, J.V. Forment, P. Cornelissen-Steijger, I. de Rink, P. ter Brugge, J.-Y. Song, S. Klarenbeek, U. McDermott, J.

Jonkers, A. Velds, D.J. Adams, D.S. Peeper, and O. Krijgsman. 2018. XenofilteR: computational deconvolution of mouse and human reads in tumor xenograft sequence data. BMC Bioinformatics. 19:366. doi:10.1186/s12859-018-2353-5.

Kozma, K.J., S.J. Done, and S.E. Egan. 2021. The tumor cell-derived matrix of lobular breast cancer: a new vulnerability. EMBO Mol. Med. 13:e13807. doi:10.15252/emmm.202013807.

Laine, R.F., I. Arganda-Carreras, R. Henriques, and G. Jacquemet. 2021. Avoiding a replication crisis in deep-learning-based bioimage analysis. Nat. Methods. 18:1136–1144. doi:10.1038/s41592-021-01284-3.

Leijnse, N., L.B. Oddershede, and P.M. Bendix. 2015. Helical buckling of actin inside filopodia generates traction. Proc. Natl. Acad. Sci. U. S. A. 112:136–141. doi:10.1073/pnas.1411761112.

Li, A., J.P. Morton, Y. Ma, S.A. Karim, Y. Zhou, W.J. Faller, E.F. Woodham, H.T. Morris, R.P. Stevenson, A. Juin, N.B. Jamieson, C.J. MacKay, C.R. Carter, H.Y. Leung, S. Yamashiro, K. Blyth, O.J. Sansom, and L.M. Machesky. 2014. Fascin is regulated by slug, promotes progression of pancreatic cancer in mice, and is associated with patient outcomes. Gastroenterology. 146:1386-1396.e1–17. doi:10.1053/j.gastro.2014.01.046.

Liao, Y., G.K. Smyth, and W. Shi. 2014. featureCounts: an efficient general purpose program for assigning sequence reads to genomic features. Bioinforma. Oxf. Engl. 30:923–930. doi:10.1093/bioinformatics/btt656.

Liu, T.-L., S. Upadhyayula, D.E. Milkie, V. Singh, K. Wang, I.A. Swinburne, K.R. Mosaliganti, Z.M. Collins, T.W. Hiscock, J. Shea, A.Q. Kohrman, T.N. Medwig, D. Dambournet, R. Forster, B. Cunniff, Y. Ruan, H. Yashiro, S. Scholpp, E.M. Meyerowitz, D. Hockemeyer, D.G. Drubin, B.L. Martin, D.Q. Matus, M. Koyama, S.G. Megason, T. Kirchhausen, and E. Betzig. 2018. Observing the cell in its native state: Imaging subcellular dynamics in multicellular organisms. Science. 360:eaaq1392. doi:10.1126/science.aaq1392.

Lodillinsky, C., E. Infante, A. Guichard, R. Chaligné, L. Fuhrmann, J. Cyrta, M. Irondelle, E. Lagoutte, S. Vacher, H. Bonsang-Kitzis, M. Glukhova, F. Reyal, I. Bièche, A. Vincent-Salomon, and P. Chavrier. 2016. p63/MT1-MMP axis is required for in situ to invasive transition in basal-like breast cancer. Oncogene. 35:344–357. doi:10.1038/onc.2015.87.

Lord, S.J., K.B. Velle, R.D. Mullins, and L.K. Fritz-Laylin. 2020. SuperPlots: Communicating reproducibility and variability in cell biology. J. Cell Biol. 219. doi:10.1083/jcb.202001064.

Lu, J., A.D. Doyle, Y. Shinsato, S. Wang, M.A. Bodendorfer, M. Zheng, and K.M. Yamada. 2020. Basement Membrane Regulates Fibronectin Organization Using Sliding Focal Adhesions Driven by a Contractile Winch. Dev. Cell. 52:631-646.e4. doi:10.1016/j.devcel.2020.01.007.

Lukinavičius, G., C. Blaukopf, E. Pershagen, A. Schena, L. Reymond, E. Derivery, M. Gonzalez-Gaitan, E. D'Este, S.W. Hell, D. Wolfram Gerlich, and K. Johnson. 2015. SiR–Hoechst is a far-red DNA stain for live-cell nanoscopy. Nat. Commun. 6:8497. doi:10.1038/ncomms9497.

Malandrino, A., X. Trepat, R.D. Kamm, and M. Mak. 2019. Dynamic filopodial forces induce accumulation, damage, and plastic remodeling of 3D extracellular matrices. PLOS Comput. Biol. 15:e1006684. doi:10.1371/journal.pcbi.1006684.

Matsubayashi, Y., B.J. Sánchez-Sánchez, S. Marcotti, E. Serna-Morales, A. Dragu, M.-C. Díaz-de-la-Loza, G. Vizcay-Barrena, R.A. Fleck, and B.M. Stramer. 2020. Rapid Homeostatic Turnover of Embryonic ECM during Tissue Morphogenesis. Dev. Cell. 54:33-42.e9. doi:10.1016/j.devcel.2020.06.005.

McCarthy, D.J., Y. Chen, and G.K. Smyth. 2012. Differential expression analysis of multifactor RNA-Seq experiments with respect to biological variation. Nucleic Acids Res. 40:4288–4297. doi:10.1093/nar/gks042.

Messal, H.A., J. van Rheenen, and C.L.G.J. Scheele. 2021. An Intravital Microscopy Toolbox to Study Mammary Gland Dynamics from Cellular Level to Organ Scale. J. Mammary Gland Biol. Neoplasia. 26:9–27. doi:10.1007/s10911-021-09487-2.

Miihkinen, M., M.L.B. Grönloh, A. Popović, H. Vihinen, E. Jokitalo, B.T. Goult, J. Ivaska, and G. Jacquemet. 2021. Myosin-X and talin modulate integrin activity at filopodia tips. Cell Rep. 36:109716. doi:10.1016/j.celrep.2021.109716.

Millard, T.H., and P. Martin. 2008. Dynamic analysis of filopodial interactions during the zippering phase of Drosophila dorsal closure. Dev. Camb. Engl. 135:621–626. doi:10.1242/dev.014001.

Miller, F.R., S.J. Santner, L. Tait, and P.J. Dawson. 2000. MCF10DCIS.com xenograft model of human comedo ductal carcinoma in situ. J. Natl. Cancer Inst. 92:1185–1186.

Monteiro, P., C. Rossé, A. Castro-Castro, M. Irondelle, E. Lagoutte, P. Paul-Gilloteaux, C. Desnos, E. Formstecher, F. Darchen, D. Perrais, A. Gautreau, M. Hertzog, and P. Chavrier. 2013. Endosomal WASH and exocyst complexes control exocytosis of MT1-MMP at invadopodia. J. Cell Biol. 203:1063–1079. doi:10.1083/jcb.201306162.

Naba, A., K.R. Clauser, H. Ding, C.A. Whittaker, S.A. Carr, and R.O. Hynes. 2016. The extracellular matrix: Tools and insights for the "omics" era. Matrix Biol. J. Int. Soc. Matrix Biol. 49:10–24. doi:10.1016/j.matbio.2015.06.003.

Naba, A., K.R. Clauser, S. Hoersch, H. Liu, S.A. Carr, and R.O. Hynes. 2012. The matrisome: in silico definition and in vivo characterization by proteomics of normal and tumor extracellular matrices. Mol. Cell. Proteomics MCP. 11:M111.014647. doi:10.1074/mcp.M111.014647.

Naba, A., K.R. Clauser, J.M. Lamar, S.A. Carr, and R.O. Hynes. 2014. Extracellular matrix signatures of human mammary carcinoma identify novel metastasis promoters. eLife. 3:e01308. doi:10.7554/eLife.01308.

Naba, A., O.M.T. Pearce, A. Del Rosario, D. Ma, H. Ding, V. Rajeeve, P.R. Cutillas, F.R. Balkwill, and R.O. Hynes. 2017. Characterization of the Extracellular Matrix of

Normal and Diseased Tissues Using Proteomics. J. Proteome Res. 16:3083–3091. doi:10.1021/acs.jproteome.7b00191.

Postma, M., and J. Goedhart. 2019. PlotsOfData—A web app for visualizing data together with their summaries. PLOS Biol. 17:e3000202. doi:10.1371/journal.pbio.3000202.

Riedl, J., A.H. Crevenna, K. Kessenbrock, J.H. Yu, D. Neukirchen, M. Bista, F. Bradke, D. Jenne, T.A. Holak, Z. Werb, M. Sixt, and R. Wedlich-Soldner. 2008. Lifeact: a versatile marker to visualize F-actin. Nat. Methods. 5:605–607. doi:10.1038/nmeth.1220.

Ritchie, M.E., B. Phipson, D. Wu, Y. Hu, C.W. Law, W. Shi, and G.K. Smyth. 2015. limma powers differential expression analyses for RNA-sequencing and microarray studies. Nucleic Acids Res. 43:e47. doi:10.1093/nar/gkv007.

Sandquist, J.C., M.E. Larson, S. Woolner, Z. Ding, and W.M. Bement. 2018. An interaction between myosin-10 and the cell cycle regulator Wee1 links spindle dynamics to mitotic progression in epithelia. J. Cell Biol. 217:849–859. doi:10.1083/jcb.201708072.

Sato, Y., K. Nagatoshi, A. Hamano, Y. Imamura, D. Huss, S. Uchida, and R. Lansford. 2017. Basal filopodia and vascular mechanical stress organize fibronectin into pillars bridging the mesoderm-endoderm gap. Development. 144:281–291. doi:10.1242/dev.141259.

Schindelin, J., I. Arganda-Carreras, E. Frise, V. Kaynig, M. Longair, T. Pietzsch, S. Preibisch, C. Rueden, S. Saalfeld, B. Schmid, J.-Y. Tinevez, D.J. White, V. Hartenstein, K. Eliceiri, P. Tomancak, and A. Cardona. 2012. Fiji: an open-source platform for biological-image analysis. Nat. Methods. 9:676–682. doi:10.1038/nmeth.2019.

Schmidt, U., M. Weigert, C. Broaddus, and G. Myers. 2018. Cell Detection with Star-Convex Polygons. In Medical Image Computing and Computer Assisted Intervention – MICCAI 2018. A.F. Frangi, J.A. Schnabel, C. Davatzikos, C. Alberola-López, and G. Fichtinger, editors. Springer International Publishing, Cham. 265–273.

Schneider, C.A., W.S. Rasband, and K.W. Eliceiri. 2012. NIH Image to ImageJ: 25 years of image analysis. Nat. Methods. 9:671–675. doi:10.1038/nmeth.2089.

Sflomos, G., L. Battista, P. Aouad, F. De Martino, V. Scabia, A. Stravodimou, A. Ayyanan, A. Ifticene-Treboux, P. Bucher, M. Fiche, G. Ambrosini, and C. Brisken. 2021. Intraductal xenografts show lobular carcinoma cells rely on their own extracellular matrix and LOXL1. EMBO Mol. Med. 13:e13180. doi:10.15252/emmm.202013180.

Shibue, T., M.W. Brooks, M.F. Inan, F. Reinhardt, and R.A. Weinberg. 2012. The outgrowth of micrometastases is enabled by the formation of filopodium-like protrusions. Cancer Discov. 2:706–721. doi:10.1158/2159-8290.CD-11-0239.

Shibue, T., M.W. Brooks, and R.A. Weinberg. 2013. An integrin-linked machinery of cytoskeletal regulation that enables experimental tumor initiation and metastatic colonization. Cancer Cell. 24:481–498. doi:10.1016/j.ccr.2013.08.012.

Singh, P., C. Carraher, and J.E. Schwarzbauer. 2010.

Assembly of Fibronectin Extracellular Matrix. Annu. Rev. Cell Dev. Biol. 26:397–419. doi:10.1146/annurev-cellbio-100109-104020.

Stubb, A., R.F. Laine, M. Miihkinen, H. Hamidi, C. Guzmán, R. Henriques, G. Jacquemet, and J. Ivaska. 2020. Fluctuation-Based Super-Resolution Traction Force Microscopy. Nano Lett. 20:2230–2245. doi:10.1021/acs.nanolett.9b04083.

Summerbell, E.R., J.K. Mouw, J.S.K. Bell, C.M. Knippler, B. Pedro, J.L. Arnst, T.O. Khatib, R. Commander, B.G. Barwick, J. Konen, B. Dwivedi, S. Seby, J. Kowalski, P.M. Vertino, and A.I. Marcus. 2020. Epigenetically heterogeneous tumor cells direct collective invasion through filopodia-driven fibronectin micropatterning. Sci. Adv. 6:eaaz6197. doi:10.1126/sciadv.aaz6197.

Tinevez, J.-Y., N. Perry, J. Schindelin, G.M. Hoopes, G.D. Reynolds, E. Laplantine, S.Y. Bednarek, S.L. Shorte, and K.W. Eliceiri. 2017. TrackMate: An open and extensible platform for single-particle tracking. Methods San Diego Calif. 115:80–90. doi:10.1016/j.ymeth.2016.09.016.

Tokuo, H., J. Bhawan, and L.M. Coluccio. 2018. Myosin X is required for efficient melanoblast migration and melanoma initiation and metastasis. Sci. Rep. 8:10449. doi:10.1038/s41598-018-28717-y.

Valenzuela, J.I., and F. Perez. 2020. Localized Intercellular Transfer of Ephrin-As by Trans-endocytosis Enables Long-Term Signaling. Dev. Cell. 52:104-117.e5. doi:10.1016/j.devcel.2019.11.013.

Vignjevic, D., M. Schoumacher, N. Gavert, K.-P. Janssen, G. Jih, M. Laé, D. Louvard, A. Ben-Ze'ev, and S. Robine. 2007. Fascin, a Novel Target of β-Catenin-TCF Signaling, Is Expressed at the Invasive Front of Human Colon Cancer. Cancer Res. 67:6844–6853. doi:10.1158/0008-5472.CAN-07-0929.

Wortel, I.M.N., K. Dannenberg, J.C. Berry, M.J. Miller, and J. Textor. 2019. CelltrackR: an R package for fast and flexible analysis of immune cell migration data. Bioinformatics.

Yurchenco, P.D., and B.L. Patton. 2009. Developmental and pathogenic mechanisms of basement membrane assembly. Curr. Pharm. Des. 15:1277–1294. doi:10.2174/138161209787846766.

Supplementary Information

Movie Legends.

Video 1. shCTRL and shMYO10 MCF10DCIS.com cells, labeled with Sir-DNA, migrating through a collagen gel were recorded using a spinning-disk confocal microscope (20x objective). Cells were then automatically tracked using StarDist and TrackMate. Raw data and Local tracks are displayed. Colour indicates ID.

Video 2. shCTRL and shMYO10 MCF10DCIS.com cells migrating through a collagen gel were recorded using a spinning-disk confocal microscope (100x objective) to visualize the protrusions generated at the invasive front.

Video 3. Various shCTRL and shMYO10 DCIS.com cell lines were mixed in different combinations so that one of the cell lines is always GFP positive, and their migration was recorded live on a spinning-disk confocal microscope (20x). The GFP-positive cells (green) and the invasive edge (magenta) were thresholded using Fiji (bottom panels).

Video 4. shCTRL^{GFP} + shMYO10 DCIS.com cells were xenografted in NOD.scid mice in 1:1 ratio. After 25 to 35 days, the resulting xenografts were imaged by intravital tile scan imaging. The 3D reconstruction was performed using the LAS X 3D Visualization module.

Video 5. shCTRL + shMYO10^{GFP} DCIS.com cells were xenografted in NOD.scid mice in 1:1 ratio. After 25 to 35 days, the resulting xenografts were imaged by intravital tile scan imaging. The 3D reconstruction was performed using the LAS X 3D Visualization module.

Video 6. DCIS.com cells were seeded as single cells in Matrigel. They were allowed to form spheroid for three days in the presence of fluorescently labeled fibronectin. Spheroids were then imaged live using a spinning-disk confocal microscope (63X). Images were then denoised using DecoNoising implemented within ZeroCostDL4Mic.

Video 7. Freshly dissected day 25 DCIS-like xenografts (green) were imaged live ex-vivo in the presence of CNA35-GFP (magenta) using a spinning-disk confocal microscope (40X, ORCA camera). The 3D reconstruction was performed using Arivis Vision4D.

Video 8. Freshly dissected day 25 shCTRL DCIS-like xenografts were imaged live ex-vivo using a spinning-disk confocal microscope (40X, ORCA camera). The 3D reconstruction was performed using Arivis Vision4D.

Video 9. Freshly dissected day 25 shMYO10 DCIS-like xenografts were imaged live ex-vivo using a spinning-disk confocal microscope (40X, ORCA camera). The 3D reconstruction was performed using Arivis Vision4D.

Video 10. shCTRL^{GFP} were injected s.c. with non-GFP shMYO10 cells and imaged with intravital microscopy through a skin flap 34 days post-tumor inoculation. Scale bar: 30 µm, interval 5 min; duration 3 hours 20 min.
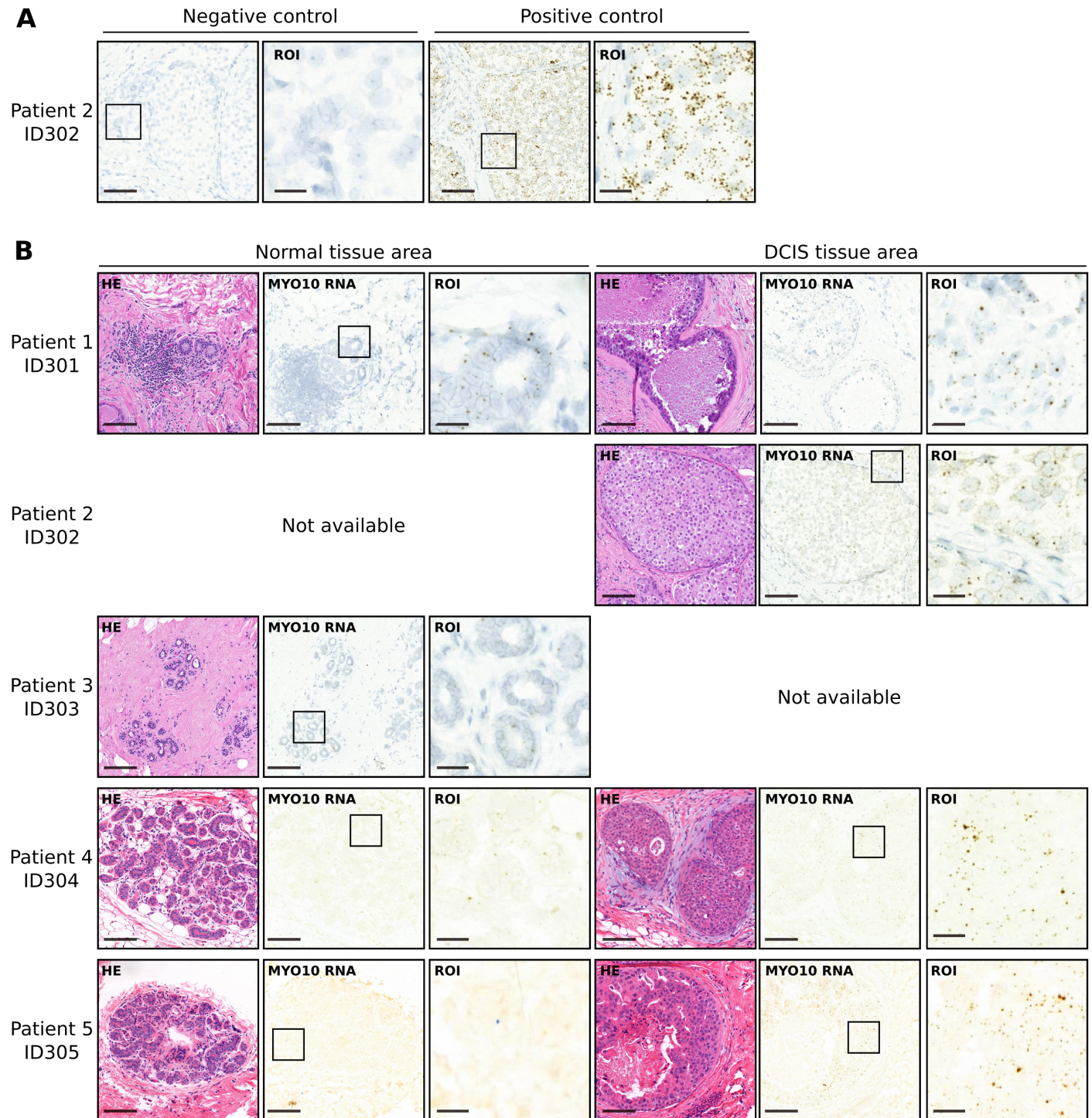
Fig. S1. MYO10 mRNA expression in patients undergoing lumpectomy after DCIS diagnosis. (**A**): Representative images of RNA in situ labeling with negative (DapB) and positive (Hs-PPIB) control probes in DCIS regions of a human breast sample (nuclei labeled with hematoxylin). RNA can be visualized by the dots visible in the magnified ROI.) Negative and positive controls were included in all independent experiments. (**B**): Representative RNA in situ labeling of MYO10 mRNA in normal and DCIS regions of a human breast sample (4 patient samples per condition). MYO10 mRNA can be visualized by the dots visible in the magnified ROI. Patient 2 sample did not contain any areas of normal breast, and patient 3 did not have DCIS despite the initial diagnosis. Elevated MYO10 expression was detected in DCIS areas compared to histologically normal breast tissue. Scale bars: (main) 100 μm; (inset) 20 μm.
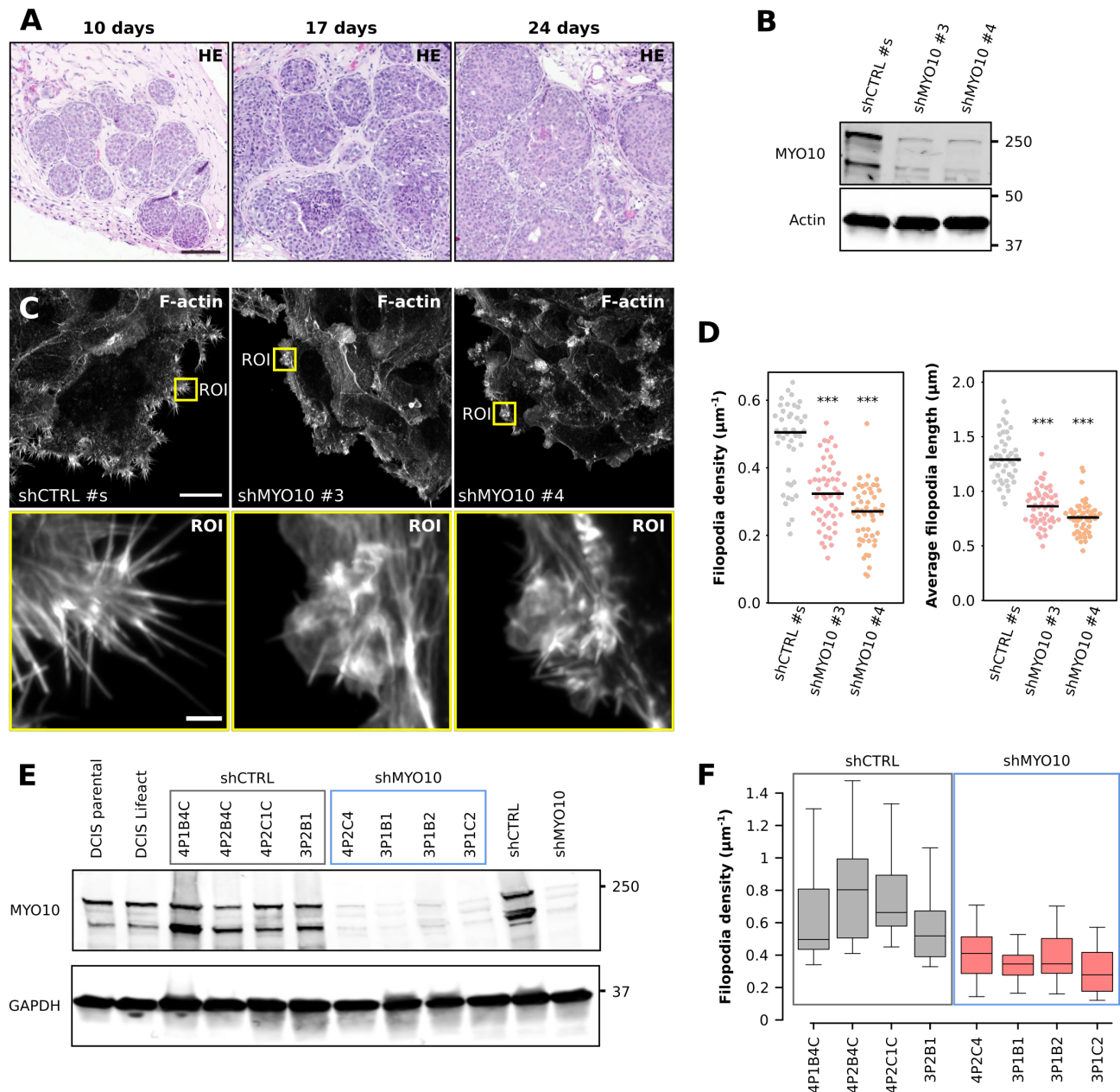
Fig. S2. MYO10 is expressed in DCIS.com cells and modulates filopodia formation. (**A**): DCIS.COM cells were injected subcutaneously in NOD.scid mice. The resulting tumors were dissected ten, 17, or 24 d post-injection. Tumor sections were then stained using HE and imaged. Representative images are displayed—scale bars: 100 µm. (**B**): DCIS.COM cells were infected with lentiviruses containing shRNA targeting MYO10 or CTRL shRNA. After antibiotic selection, cells were lysed, and MYO10 protein levels were analyzed by western blot. (**C-D**): DCIS.COM cells generated in (**B**) were left to migrate underneath a collagen gel for 2 d, fixed, stained, and imaged using a spinning-disk confocal microscope. (**C**): Representative fields of view are displayed showing the morphology of shCTRL #s, shMYO10 #3, and shMYO10 #4 cells. Yellow squares highlight ROIs that are magnified. Scale bars: (main) 25 µm; (inset) 2 µm. (**D**): Filopodia density and the average filopodia length were analyzed using FiloQuant. Results from three independent experiments are displayed as dot plots (n > 44 fields of view analyzed per condition; *** p-value < 0.001, randomization test). (**E-F**): Single-cell clones were isolated from the cell lines generated in (B), and their MYO10 protein levels were compared to parental DCIS.com cells by western blot. (**E**): Four clones with low MYO10 expression and four clones with high MYO10 expression were mixed to generate the shMYO10 and shCTRL cell lines, respectively. (**F**): Filopodia density for each single cell clone was automatically analyzed using FiloQuant. Results are displayed as box plots (n > 20 fields of view analyzed per condition; two independent experiments).
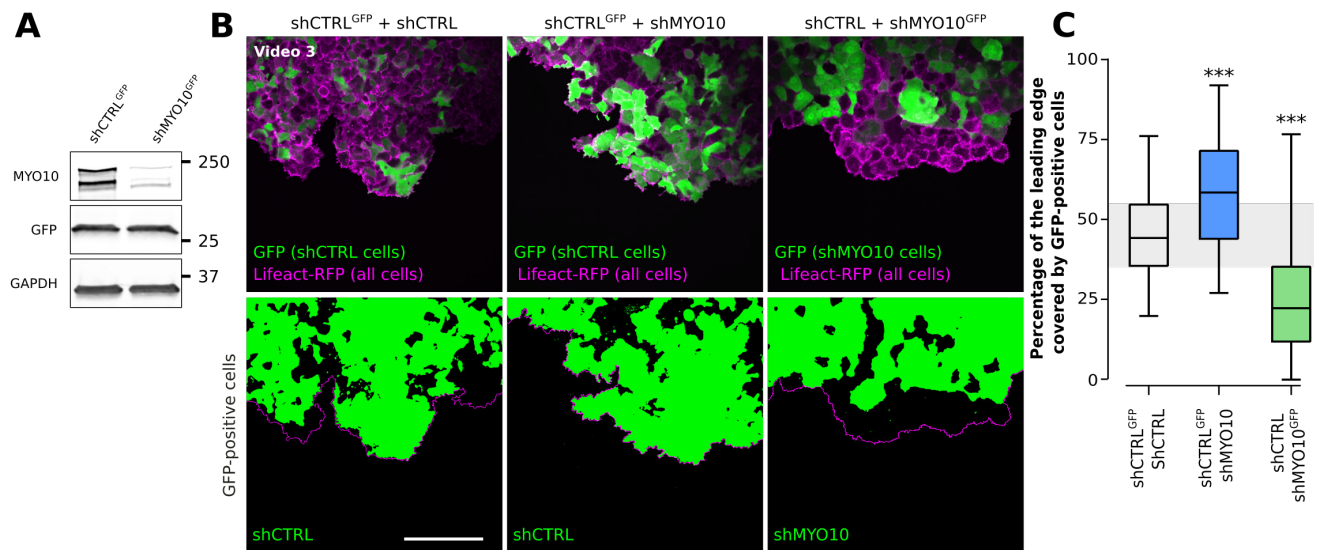
Fig. S3. Figure S3: MYO10 promotes cell migration in DCIS.com cells *in vitro*. (**A**): shCTRL and shMYO10 DCIS.com cells were infected with GFP-containing lentiviruses, lysed, and their MYO10 and GFP expression levels were analyzed by western blots. A representative western blot is displayed. (**B-C**): Various shCTRL and shMYO10 DCIS.com cell lines were mixed in different combinations so that one of the cell lines is always GFP positive, and cell migration was recorded live on a spinning-disk confocal microscope (20x). Representative images are displayed (see also Video 3). Scale bar: 200 μm. For each condition, the percentage of the leading edge covered by GFP-positive cells was measured using Fiji. (**C**): The results are displayed as Tukey box plots (n > 5266 fields of view analyzed per condition; 3 biological repeats; *** p-value < 0.001, randomization test).
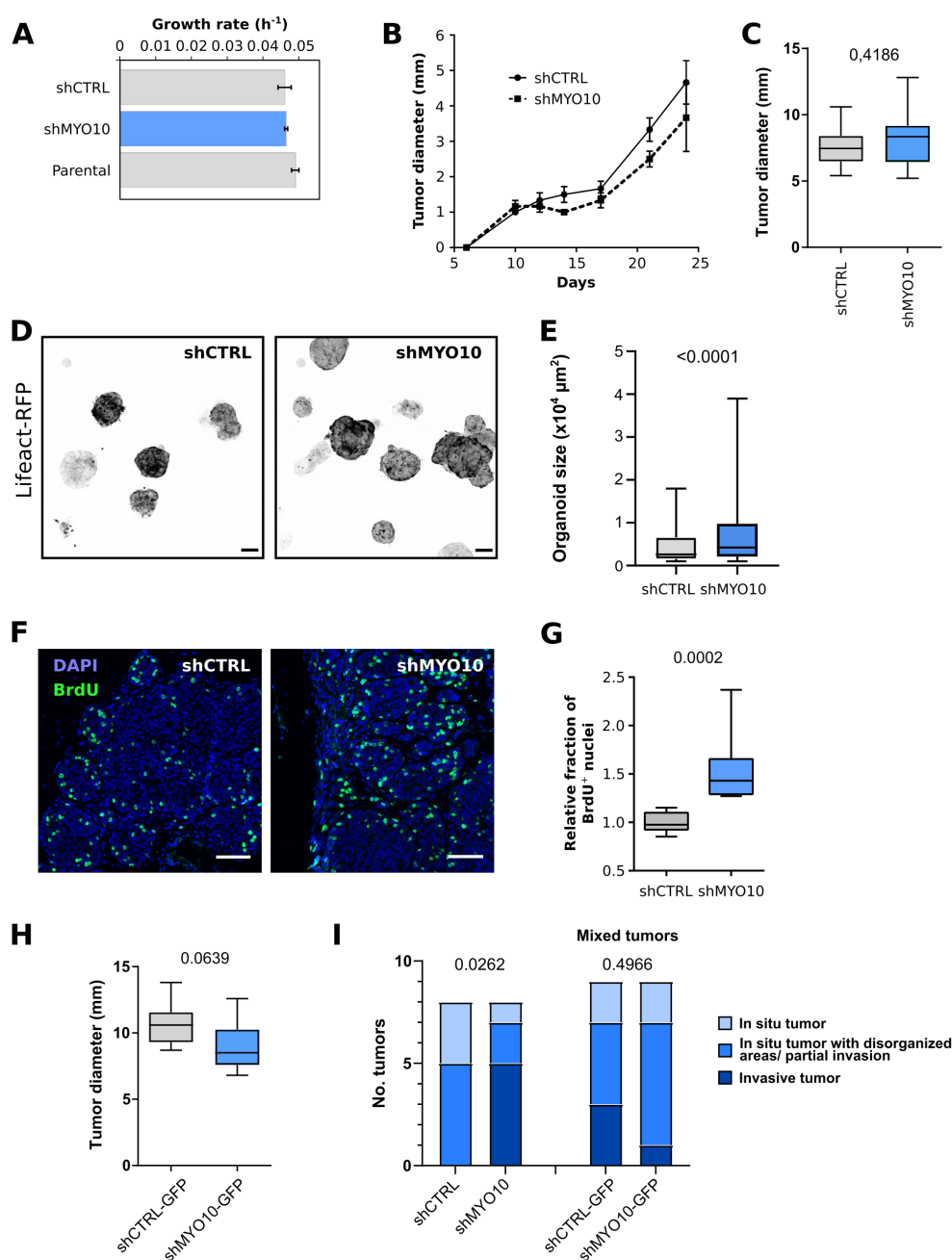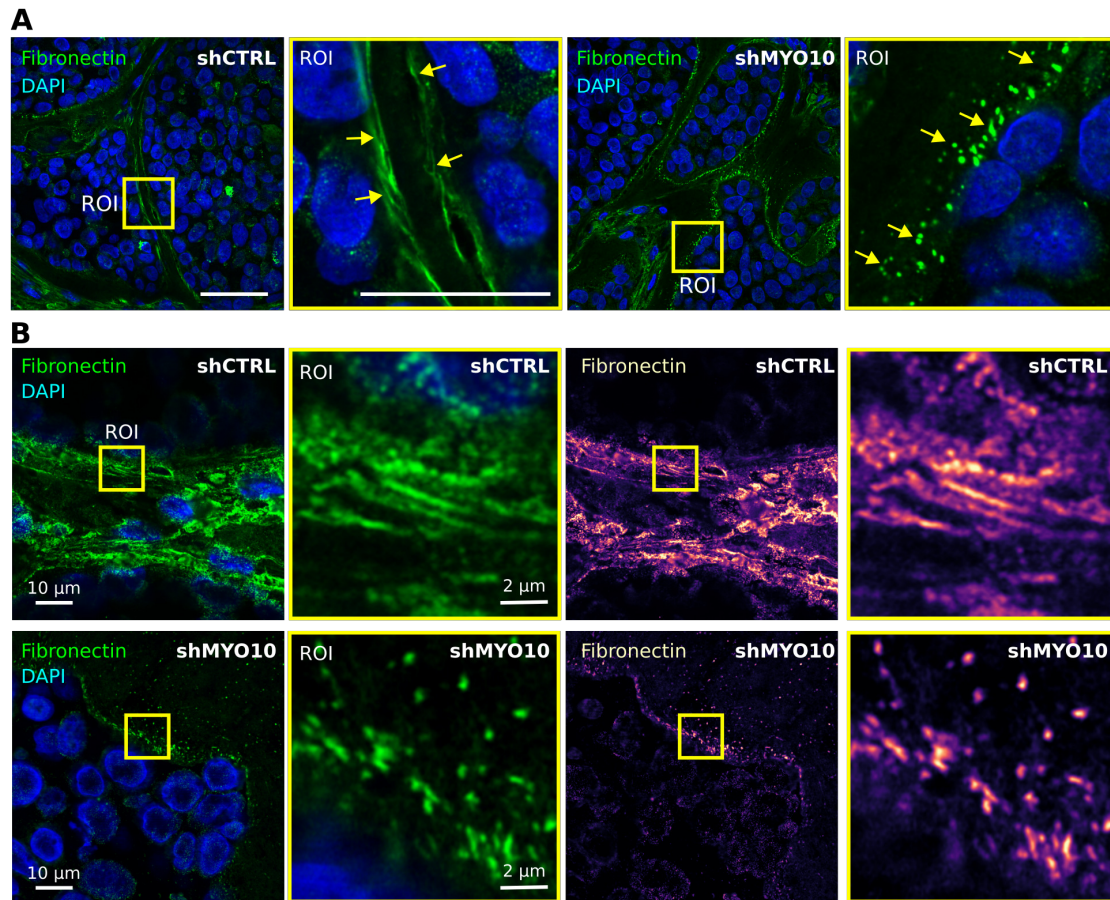
Fig. S4. MYO10 is not required for DCIS.com cells proliferation *in vitro* or *in vivo*. (**A**): shCTRL and shMYO10 cells were plated in a six-well plate, and their proliferation rate was recorded using an incubator microscope (three biological repeats, error bars indicate SEM). (**B-D**): shCTRL and shMYO10 cells were injected subcutaneously in NOD.scid mice, and the tumor diameter was followed over time (n= 6 tumors) (**B**). At 25 days post-injections, the tumors were dissected and their maximum diameter measured (n=12 tumors, from 3 independent experiments, unpaired t-test) (**C**). (**D-E**): shCTRL and shMYO10 cells were seeded as single cells in a mixture of 70% matrigel 30% collagen I and allowed to form spheroids for seven days. (**D**): Fixed samples were imaged using lifeact-RFP fluorescence and a confocal microscope. (**E**): Spheroid area was measured using Fiji (see methods for details). Scale bars: 50 μm. Results are displayed as Tukey box plots (six biological repeats per condition, fields of view analyzed per experiment; nshCTRL =132; nshMYO10 =179; Mann-Whitney test). (F-G): shCTRL and shMYO10 DCIS-like xenograft sections were analyzed 25 days post-injection for BrdU incorporation to assess tumor proliferation. (**F**): Representative fields of view are displayed. Scale Bar: 100 μm. (**G**): The fraction of BrdU labeled nuclear area in each field of view was normalized to shCTRL average. Results are shown as box plots (n=8 tumors from two independent experiments, Mann-Whitney test). (**H-I**): shCTRLGFP + shMYO10 or shMYO10GFP + shCTRL DCIS.com cells were xenografted in NOD.scid mice in 1:1 ratio. (**H**): At 25 days post-injections, the tumors were dissected and their maximum diameter measured (n=9 tumors, unpaired t-test). (**I**): Tissue sections were stained with HE and imaged. Scoring of DCIS invasion is shown in mixed tumors (n=9 tumors) compared to the invasion of shCTRL and shMYO10 tumors (n = 8 tumors; Chi-square test).
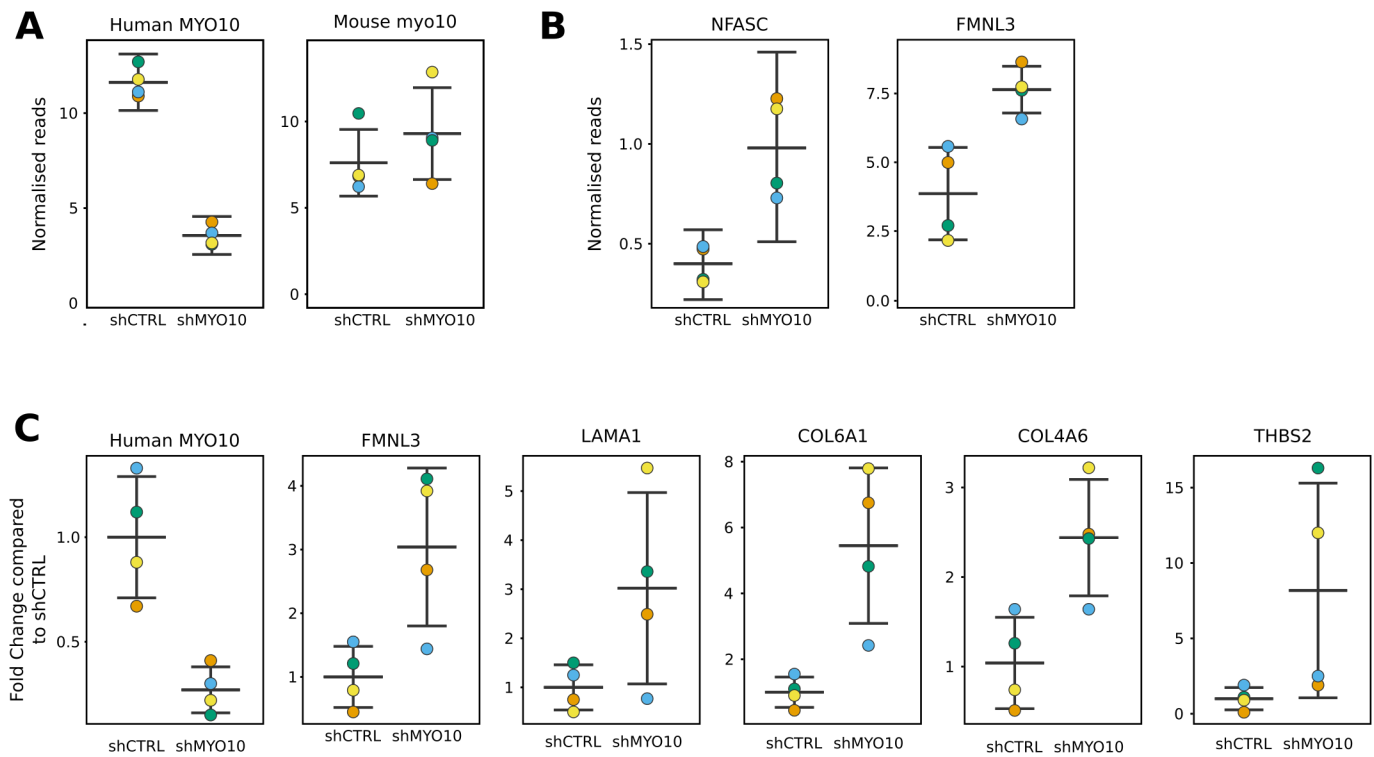
Fig. S5. MYO10 modulates fibronectin assembly *in vivo*. (**A-B**): Ten-day-old shCTRL and shMYO10 DCIS-like xenografts were stained for DAPI and fibronectin and imaged using a spinning-disk confocal microscope (**A**, 63x objective) or at high resolution using an Airyscan confocal microscope (**B**). Representative fields of view are displayed. Yellow squares indicate ROIs that are magnified. (**A**): Scale bars: (main) 50 µm; (inset) 25 µm. (**B**): Scale bars: (main) 10 µm; (inset) 2 µm.

Fig. S6. MYO10 silencing drives the expression of filopodia-inducing and ECM genes. (**A-C**): The expression levels of multiple genes (as indicated) were measured in 25-day-old shCTRL and shMYO10 DCIS-like xenografts using RNAseq (**A**, **B**) or qPCR (**C**), and results are displayed as SuperPlots (Lord et al., 2020; Goedhart, 2021). N = 4 mice per condition.
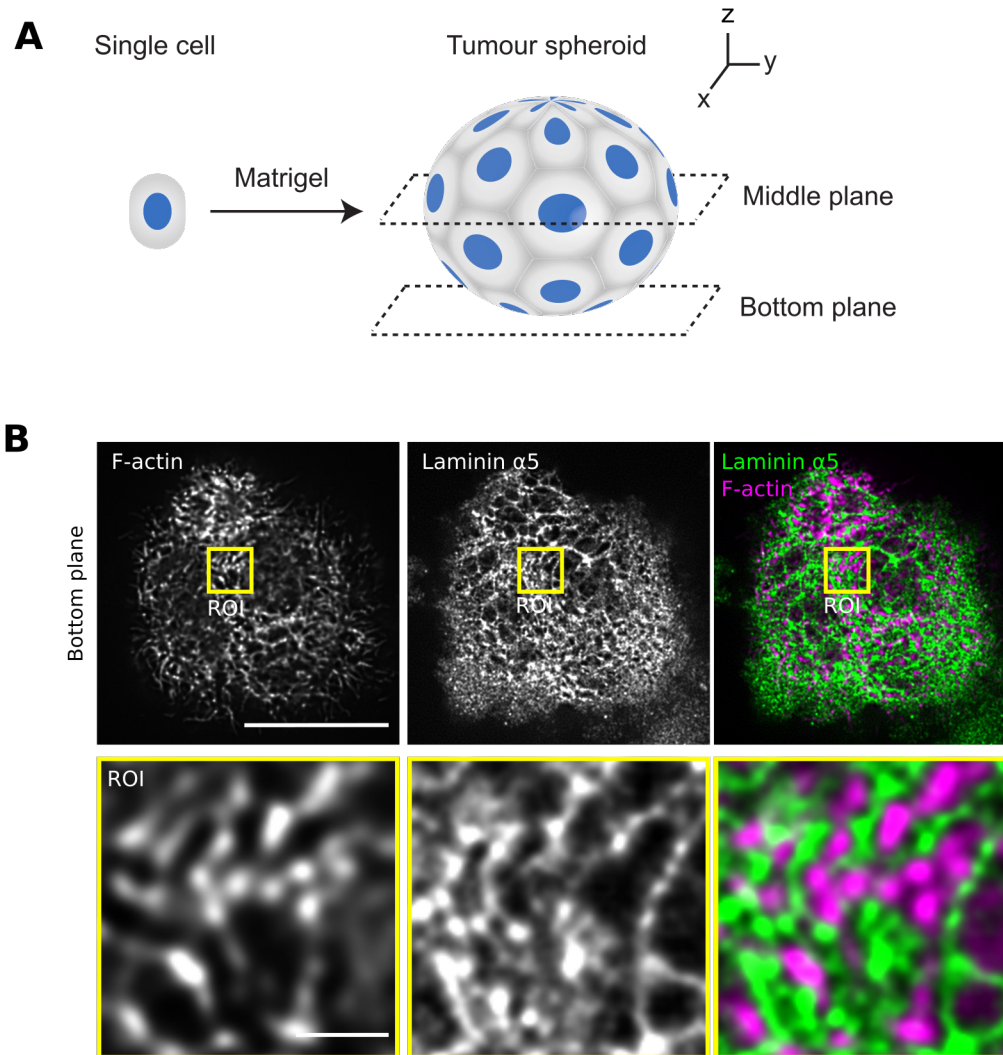
Fig. S7. ECM assembly in 3D spheroids. (**A**): Schematic presentation of the spheroid protocol. (**B**): DCIS.com cells were seeded as single cells in Matrigel. They were allowed to form spheroids for three days in the presence of fluorescently labeled laminin α5. Samples were fixed and imaged using a spinning-disk confocal microscope and processed using eSRRF. A representative field of view highlighting a spheroid's bottom plane is displayed. Scale bars: (main) 25 μm; (inset) 5 μm. Yellow squares indicate ROIs that are magnified.